

# Analytical methods to determine the effective mesoscopic and macroscopic elastic properties of cortical bone

William J. Parnell · M. B. Vu · Q. Grimal · S. Naili

Received: 18 April 2011 / Accepted: 2 November 2011 / Published online: 23 November 2011  
© Springer-Verlag 2011

**Abstract** We compare theoretical predictions of the effective elastic moduli of cortical bone at both the meso- and macroscales. We consider the efficacy of three alternative approaches: the method of asymptotic homogenization, the Mori–Tanaka scheme and the Hashin–Rosen bounds. The methods concur for specific engineering moduli such as the axial Young’s modulus but can vary for others. In a past study, the effect of porosity alone on mesoscopic properties of cortical bone was considered, taking the matrix to be isotropic. Here, we consider the additional influence of the transverse isotropy of the matrix. We make the point that micromechanical approaches can be used in two alternative ways to predict either the macroscopic (size of cortical bone sample) or mesoscopic (in between micro- and macroscales) effective moduli, depending upon the choice of representative volume element size. It is widely accepted that the mesoscale behaviour is an important aspect of the mechanical behaviour of bone but models incorporating its effect have started to appear only relatively recently. Before this only macroscopic behaviour was addressed. Comparisons are drawn with experimental data and simulations from the literature for macroscale predictions with particularly good agreement in the case of dry bone. Finally, we show how predictions of the effective

mesoscopic elastic moduli can be made which retain dependence on the well-known porosity gradient across the thickness of cortical bone.

**Keywords** Cortical bone · Asymptotic homogenization and micromechanics · Transverse isotropy · Porosity · Mesoscale · Macroscale

## 1 Introduction

From the mechanical point of view, bone is a relatively hard and lightweight composite material which, at deeper observation, presents a hierarchy of microstructures. Indeed, the exceptional mechanical properties of bone are mainly due to its specific hierarchical structure and composition. From the visible scale down to the nanometre one, it is possible to distinguish: cancellous and cortical tissues, Haversian systems and osteons, lamellae, collagen fibres, collagen fibrils, and elementary constituents (collagen, mineral, water, etc.). From the compositional point of view, elementary constituents of bone are the following: an organic phase, mainly made up of type-I collagen; a mineral phase, essentially composed of hydroxyapatite crystals; a fluid phase (water and other organic fluids), partially filling the micro- and macroporosities.

In a purely macroscopic approach, the existence of a representative volume element (RVE) must in general be postulated so that the macroscopic constitutive laws derived experimentally or ad hoc theoretically, using general thermodynamic constraints, represent the response of the RVE to various loadings. Such a treatment is well suited in various scenarios in the science and engineering domains; in particular, this is adequate for many natural geological and biological media. However, in various other situations,

W. J. Parnell (✉)  
School of Mathematics, University of Manchester, Alan Turing  
Building, Manchester M13 9PL, UK  
e-mail: William.Parnell@manchester.ac.uk

M. B. Vu · S. Naili  
Université Paris-Est, Laboratoire Modélisation et Simulation Multi  
Echelle, MSME UMR 8208 CNRS, 61, avenue du Général de  
Gaulle, 94010 Créteil Cedex, France

Q. Grimal  
Laboratoire d’Imagerie Paramétrique, Université Pierre et Marie Curie,  
LIP UMR 7623 CNRS, Paris 75006, France

heterogeneities present at the small (micro) scale play an important role in the general behaviour. In this case, homogenization and micromechanical methods are powerful tools not only to obtain the overall behaviour of the material via the determination of the overall properties, but also to obtain information about the microfields associated with the local distribution of the macrofields. Macroscopic predictions of either part or all of the elastic modulus tensor have been given by many authors. We note the work of [Katz \(1980\)](#) who used the Hashin–Rosen bounding scheme, [Crolet et al. \(1993\)](#) who used asymptotic homogenization and most recently ([Hamad et al. 2010](#)) who used various micromechanical methods in order to build a multiscale model of cortical bone.

In many materials, of which bone is a good example, there are a plethora of length scales, and it is possible to homogenize over some of these whilst retaining spatial dependence on a length scale which is still smaller than the macroscale. This situation will be studied in this article (as well as macroscopic homogenization) where we define the so-called *mesoscale* as defined in [Grimal et al. \(2008\)](#), [Parnell and Grimal \(2009\)](#). Dependence of homogenized properties on a characteristic length of the mesoscale has been discussed in a relatively small number of articles [see for example [Hellmich et al. \(2008\)](#), [Yosibash et al. \(2008\)](#), [Fritsch et al. \(2009\)](#)] where a combination of finite element and micromechanical models were employed. It is useful to retain the mesoscale behaviour such as the well-known porosity gradient across the cortical bone cross-section. The resulting gradient in effective properties when we homogenize the *micro* scale can then be retained in macroscopic models. Our mesoscopic homogenization approach is therefore as depicted in Fig. 2. We take a mesodomain “window” in the cross-section of cortical bone, associate a given level of porosity with this mesodomain, and then homogenize this local mesodomain by considering its idealization as a doubly periodic structure. Moving this window then gives rise to the variation in effective properties across the cortical bone cross-section.

In the present paper we use the method of asymptotic homogenization (MAH), assuming that the pores in the local region of interest are periodically distributed within the matrix material, specifically on a hexagonal lattice, which leads to a transversely isotropic material for pores with circular cross-section. This symmetry is thought to be a reasonable approximation of the effective behaviour of cortical bone ([Yoon and Katz 1976a,b](#)). Although computational methods can now be used on exact imaged microstructures of cortical bone, the subsequent large amount of data produced in such approaches is not always helpful. In particular micromechanical methods on simple geometries can assist in parametric studies.

Asymptotic homogenization is a popular and effective method for determining the effective moduli of periodic media ([Bakhvalov and Panasenko 1989](#); [Parton and](#)

[Kudryavtsev 1993](#)). The approach exploits the separation of scales within the composite material and uses the method of multiple scales in order to derive a homogenized equation governing the effective behaviour of the material in question. The approach has many advantages, which were listed in [Parnell and Grimal \(2009\)](#).

The current approach is novel and unique in the context of cortical bone modelling, due to the solution scheme of the periodic cell problem ([Parnell and Abrahams 2006, 2008](#)). The method is stable even for high porosities and high contrast phases as in the limiting cases of rigid fibres and voids. Solutions are found in terms of asymptotic expansions and so we are aware of the order of error made by assuming a leading order solution. Furthermore, the scheme does not introduce any ad hoc assumptions, which are required by the standard micromechanical methods. The classical self-consistent scheme would appear inappropriate due to its link with polycrystalline materials rather than with host-inclusion materials, although the (more complicated) generalized self-consistent scheme could be useful. Finally, although the Mori–Tanaka scheme has been shown to lie rigorously inside the Hashin–Shtrikman bounds for a single inclusion phase, for several distinct inclusion phases this scheme can give predictions which do lie outside these bounds ([Ponte-Castaneda and Willis 1995](#)), and therefore, the method should be used with great caution.

In [Parnell and Grimal \(2009\)](#), the asymptotic method was used in order to predict the influence of geometrical effects (porosity) on the induced anisotropy of cortical bone. The matrix phase was assumed to be isotropic. That study, therefore, permitted the analysis of the separate contribution to bone anisotropy due to geometrical effects alone. Furthermore, that study defined the notion of the mesoscale in cortical bone as described above and discussed its importance with respect to the variation in material properties across the cross-section of a bone sample. This work extends that of [Parnell and Grimal \(2009\)](#) in order to incorporate the transverse isotropy of the matrix phase and assess its influence on effective properties via a parameter study, considering pores as either hard (fluid filled) or soft (empty). Strictly speaking, bone is a poroelastic material, and therefore, a relevant framework with which to study the effective behaviour of the medium is that presented by [Cowin \(1999\)](#) who applied the classical Biot poroelasticity theory to study deformation driven fluid motion. However in many situations where the focus is on the effective elastic behaviour and not on the fluid motion or distribution of stress inside pores, the fluid can be considered to be at rest, or rather, we consider the fluid to a perfect (inviscid) fluid. Moreover, we note that if we did wish to derive the full effective poroelastic coefficients, then the derivation of the effective *elastic* moduli is a necessary part of this ([Dormieux et al. 2002](#); [Lydzba and Shao 2000](#)). Here we focus on the effective elastic modulus tensor, noting that

when fluid motion is taken into account, the full poroelastic framework should be used.

After this introduction on the rationale for studying homogenized mesoscopic and macroscopic elastic properties, in Sect. 2, we describe the assumptions of the current model and give brief details of the MAH in Sect. 3. For parameters within the physiological range of those of bone we carry out a parameter study in order to assess the additional influence of transverse isotropy on the effective properties of cortical bone using the MAH alone. Following this we compare the predictions of the effective properties of cortical bone with the Mori–Tanaka micromechanical method and the Hashin variational principles for inhomogeneous materials in Sect. 4 noting that porosity here can either be considered as macroscopic or mesoscopic permitting the alternative viewpoints. In Sect. 5 we compare predictions of the MAH with experimental results taken from the literature. Finally, in Sect. 6, we model mesoscopic behaviour by incorporating the porosity variation across the cross-section of cortical bone and thus predict the variation in effective properties are anisotropy ratio. We make the point that mesoscale properties can vary significantly from their macroscopic counterparts.

We place some details of the classical micromechanical methods in appendices. We do this since many such formulae are exceedingly difficult to find in the literature and are frequently stated inconsistently from one author to another. Moreover, typographical errors are often encountered.

## 2 Assumptions of the model

As in Parnell and Grimal (2009), we shall model cortical bone as a two-phase composite material, employing Cartesian coordinates where the  $x_3$ -axis runs parallel to the long axis of the bone. The mesoscale pores (Haversian canals and resorption cavities) are modelled as identical cylinders of infinite extent in the  $x_3$ -direction, and we assume that they are distributed on a hexagonal lattice in the  $x_1x_2$  plane. For ease of exposition, here, we shall consider only pores of *circular* cross-section. These pores represent Haversian canals or resorption cavities that are roughly aligned in cortical bone (Cooper et al. 2007). The proposed method can model many pores inside the periodic cell, but the idea behind this work is to retain simplicity, and hence, a single-pore model (within the periodic cell) will be retained. The fact that pores are assumed to be of “infinite extent” is in no way as grave as one may initially think. In particular it is to be noted that in micromechanical models of inhomogeneous media, aspect ratios of spheroidal inclusions (major semi-axis over minor semi-axis) ranging between 10 and 20 can be considered to be of infinite extent. This is because effective properties change only very slightly when increasing the aspect ratio beyond

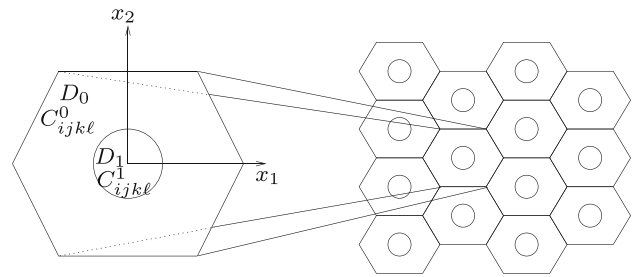


**Fig. 1** Figure showing the geometry of the assumed microstructure of an RVE at the mesoscale. Circular cylindrical pores are arranged on a hexagonal lattice. This together with the transversely isotropic matrix phase induces macroscopic transverse isotropy. Figure first published in Parnell and Grimal (2009)

this range. We refer to Rodriguez et al. (2009) for further details, results and references on this issue.

The mesoscale pores are surrounded by bony matrix tissue, which we assume to be *transversely isotropic* (TI). In Parnell and Grimal (2009) it was assumed that this phase is isotropic, and hence the induced anisotropy there is solely due to geometry. Here we shall address the induced anisotropy due to both geometry and matrix anisotropy. The hexagonal periodic cell shown in Fig. 1 contains a single circular cylindrical pore and defines the mesoscale structure in the  $x_1x_2$  plane and ensures transverse isotropy. This can be shown by imposing invariance of the elastic strain energy to rotations of  $\pi/3$  in the  $x_1x_2$  plane together with reflections in the  $x_1x_2$  plane (Sokolnikoff 1956). This periodic model material of infinite extent is thus intended to give a snapshot of the (local) effective elastic properties of bone at a specific (mesodomain) location (in the language used above) at a point in the cortical bone cross-section. The mesodomain is defined by its porosity. Later we shall give some discussion as to how we can use this method to derive the variation in elastic moduli across the thickness of bone. This is illustrated in Fig. 2 where we show how the mesostructure within the local region (mesodomain) of the cortical bone cross-section is first replaced by an idealized hexagonal structure and then homogenized by using the concept of an infinite periodic medium as described above.

The matrix and pore phases are assumed to be purely elastic with respective mass densities  $\hat{\rho}_0$  and  $\hat{\rho}_1$  and components of elastic moduli  $\hat{C}_{ijkl}^0$  and  $\hat{C}_{ijkl}^1$  respectively. The pore properties are assumed isotropic and hence can be defined by their two Lamé constants  $\lambda_1$  and  $m_1$  where the latter denotes the shear modulus. The matrix phase is considered transversely isotropic, and therefore, it possesses five independent elastic moduli. Notation for these properties will be discussed shortly.

We define the characteristic length of the microscale (for example distance between pores) as  $q$ . Within the periodic cell, the domain of the pore is denoted by  $D_1$  and the matrix

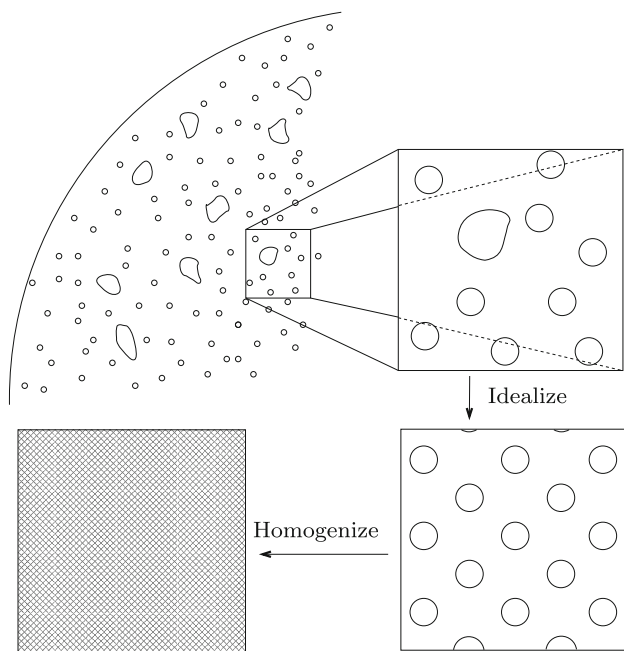


**Fig. 2** The notion of determining local effective properties. Here we have shown the mesostructure as a collection of Haversian canals (circles) and resorption cavities (slightly larger, less circular regions). The local region (RVE) in the cortical bone cross-section is analyzed and then replaced by an idealized mesostructure. This region is then homogenized by treating the medium as periodic and of infinite extent. The resulting effective properties then define the elastic behaviour of this local region. Figure first published in Parnell and Grimal (2009)

by  $D_0$ , their respective areas being denoted by  $|D_1|$  and  $|D_0|$ , and we define  $|D| = |D_0| + |D_1|$  as the total cell area.

### 3 Asymptotic homogenization and the cell problem

We employ the theory developed by Parnell and Abrahams (2006, 2008) in order to determine the effective elastic properties by modelling the propagation of low frequency elastic waves through the material. We shall summarize the findings of the theory here, but we refer the reader to these papers for more in-depth findings and details, particularly with regard to the solution of the cell problem. Neglecting body forces, the equations governing the displacement  $\mathbf{u} = (u_1, u_2, u_3)$  of time harmonic waves of angular frequency  $\omega$  (within each phase) are given by

$$\frac{\partial}{\partial \hat{x}_j} \left( \hat{C}_{ijkl}(\hat{\mathbf{x}}) \frac{\partial u_k}{\partial \hat{x}_\ell} \right) + \hat{\rho}(\hat{\mathbf{x}}) \omega^2 u_i = 0, \quad (1)$$

where the coordinates of a point  $\hat{\mathbf{x}}$  are specified by  $(\hat{x}_1, \hat{x}_2, \hat{x}_3)$ . The Einstein convention of summation over repeated *subscripts* has been adopted. In (1) introduce the non-dimensional variable  $x_i = \hat{x}_i/q$  and divide by  $\hat{C}_{1212}^0$ , the in-plane shear modulus of the matrix phase so that we obtain

$$\frac{\partial}{\partial x_j} \left( C_{ijkl}(\mathbf{x}) \frac{\partial u_k}{\partial x_\ell} \right) + \epsilon^2 \rho(\mathbf{x}) u_i = 0, \quad (2)$$

where  $\epsilon = q\kappa_s$  and  $\kappa_s^2 = \omega^2 \hat{\rho}_0 / \hat{C}_{1212}^0$  is the shear wave number of the matrix phase. We have also defined  $C_{ijkl}(\mathbf{x}) = \hat{C}_{ijkl}(\hat{\mathbf{x}}) / \hat{C}_{1212}^0$  and  $\rho(\mathbf{x}) = \hat{\rho}(\hat{\mathbf{x}}) / \hat{\rho}_0$ .

We note that  $C_{ijkl}(\mathbf{x})$  and  $\rho(\mathbf{x})$  are piecewise constant, taking the form  $C_{ijkl}(\mathbf{x}) = C_{ijkl}^r \chi_r(\mathbf{x})$  and  $\rho(\mathbf{x}) = \rho_r \chi_r(\mathbf{x})$  for  $r = 0, 1$  where  $\chi_r(\mathbf{x})$  is the characteristic function of the  $r$ th phase:

$$\chi_r(\mathbf{x}) = \begin{cases} 1, & \mathbf{x} \in D_r, \\ 0, & \mathbf{x} \notin D_r. \end{cases} \quad (3)$$

Using the description of TI tensors given in Appendix A, we can conveniently write both elastic modulus tensors in the form

$$C_{ijkl}^r = \sum_{n=1}^6 X_n^r \mathcal{H}_{ijkl}^{(n)}, \quad (4)$$

where the constants  $X_n^r$  are given by  $X_1^r = 2k_r$ ,  $X_2^r = X_3^r = \ell_r$ ,  $X_4^r = \gamma_r$ ,  $X_5^r = 2\mu_{Tr}$ ,  $X_6^r = 2\mu_{Ar}$  and the basis tensors are defined in (41)–(43). The notation used in (4) will be related to the elastic moduli  $C_{ijkl}^r$  shortly. We note in particular that  $k_r$  is the in-plane bulk modulus,  $\mu_{Tr}$  is the in-plane (transverse) shear modulus, and  $\mu_{Ar}$  is the anti-plane axial shear modulus. We reinforce that these properties have been non-dimensionalized on the in-plane shear modulus of the matrix. Since  $C_{ijkl}^0$  is fully TI, it has the following independent components

$$C_{1111}^0 = k_0 + \mu_{T0}, \quad C_{3333}^0 = \gamma_0, \quad (5)$$

$$C_{1122}^0 = k_0 - \mu_{T0}, \quad C_{2323}^0 = \mu_{A0}, \quad (6)$$

$$C_{1133}^0 = \ell_0 = k_0 - \mu_{T0} + \eta_0, \quad (7)$$

which are non-dimensional, having been scaled on  $\hat{C}_{1212}^0$ . Furthermore, we have the property  $C_{1212}^0 = (C_{1111}^0 - C_{1122}^0)/2 = \mu_{T0}$ . Pore properties are isotropic, given by

$$C_{1111}^1 = k_1 + \mu_1, \quad C_{3333}^1 = \gamma_1 = k_1 + \mu_1, \quad (8)$$

$$C_{1133}^1 = \ell_1 = k_1 - \mu_1 = C_{1122}^1, \quad C_{2323}^1 = \mu_{A1} = \mu_1, \quad (9)$$

where  $\mu_1 = m_1 / \hat{C}_{1212}^0$  and  $k_1 = (\lambda_1 + m_1) / \hat{C}_{1212}^0$ . Since we assume that we are in the low-frequency regime where the wavelength of the propagating waves is much larger than the mesoscale  $q$ , we can assume that  $\epsilon \ll 1$ . Therefore, a so-called separation of scales exists, and we can perform asymptotic homogenization. We assume boundary conditions on the pore/matrix interface  $\partial D_1$  of continuity of displacement and traction, i.e.

$$[u_i]_\pm^+ = 0, \quad [\sigma_{ij} n_j]_\pm^+ = 0, \quad i = 1, 2, 3, \quad (10)$$

where  $\sigma_{ij}$  is the Cauchy stress tensor,  $n_j$  is the  $j$ th component of the normal to  $\partial D_1$  (pointing into the matrix) and where



we have used the notation  $[f(z)]_+^+$  to denote the jump in the function  $f(z)$  across  $\partial D_1$ .

To determine leading order quasi-static behaviour, MAH proceeds by defining the multiple scale variables

$$x_\alpha = \xi_\alpha, \quad \alpha = 1, 2, \quad x_j = \frac{z_j}{L(\epsilon)}, \quad j = 1, 2, 3, \quad (11)$$

where  $L(\epsilon) = \epsilon + L_2\epsilon^2 + \dots$ , an expansion which is required if one wishes to determine higher-order terms associated with dynamic homogenization (Parnell and Abrahams 2006). On introducing  $\xi = (\xi_1, \xi_2)$  and  $\mathbf{z} = (z_1, z_2, z_3)$  we note from (11) that these are short and long lengthscales respectively. No mesovvariable is required in the long bone axis direction and thus (11) imply that

$$\frac{\partial}{\partial x_\alpha} = \frac{\partial}{\partial \xi_\alpha} + L(\epsilon) \frac{\partial}{\partial z_\alpha}, \quad \alpha = 1, 2, \quad \frac{\partial}{\partial x_3} = L(\epsilon) \frac{\partial}{\partial z_3}. \quad (12)$$

Note that in the following, Greek indices run from 1 to 2 whereas Latin insides run from 1 to 3.

An expansion in  $\epsilon$  is performed for the displacements

$$u_k(\xi, \mathbf{z}) = u_{k0}(\xi, \mathbf{z}) + \epsilon u_{k1}(\xi, \mathbf{z}) + \dots \quad (13)$$

Since the material is doubly periodic (with hexagonal symmetry) with respect to  $\xi$ , we insist that each  $u_{kj}$  is doubly periodic in  $\xi$  on the hexagonal lattice.

Substituting (11)–(13) into the governing equations (2) and boundary conditions (10) and equating orders in  $\epsilon$ , we obtain a hierarchy of problems, one associated with each order in  $\epsilon$  (Bakhvalov and Panasenko 1989). As is usual in the theory of homogenization for elastodynamics, the  $O(1)$  problem shows that the leading order displacement field is (explicitly) independent of  $\xi$  so that  $u_{k0}(\xi, \mathbf{z}) = U_k(\mathbf{z})$ . At  $O(\epsilon)$  it turns out that it is advantageous to write the solution in the separable form

$$u_{k1}(\xi, \mathbf{z}) = N_k^{pm}(\xi) \frac{\partial U_p(\mathbf{z})}{\partial z_m}. \quad (14)$$

This form then gives rise to the resulting *cell problems* for  $N_k^{pm}(\xi)$ . As we shall show in (18)–(24) below, since the superscripts  $p$  and  $m$  merely alter the *forcing* in the boundary conditions of the cell problem, it is useful to employ bold font notation  $\mathbf{N}_k$  so that  $N_k^{pm}$  corresponds to the  $(p, m)$ th component of  $\mathbf{N}_k$ . For TI phases, on denoting the derivative of  $\mathbf{N}_k$  with respect to  $\xi_\alpha$  by  $\mathbf{N}_{k,\alpha}$  it turns out that the governing equations for the cell problems (in the  $r$ th phase) are of the form Parnell and Abrahams (2008)

$$k_r \mathbf{N}_{\alpha,\beta\alpha}^r + \mu_{Tr} \mathbf{N}_{\beta,\alpha\alpha}^r = 0, \quad \beta = 1, 2, \quad (15)$$

$$\mu_{Ar} \mathbf{N}_{3,\alpha\alpha}^r = 0, \quad (16)$$

for  $r = 0, 1$  and where the superscript  $r$  on  $\mathbf{N}_k^r$  refers to the  $r$ th phase. It is noted that these governing equations of the cell problems are of exactly the same form as those for *isotropic*

phases as described in Parnell and Grimal (2009) (except for the distinction between  $\mu_{Ar}$  and  $\mu_{Tr}$  since  $\mu = \mu_T = \mu_A$  in the isotropic case). The main difference for TI media can be seen as a subtle change in the boundary conditions which are

$$\mathbf{N}_k^0|_{\partial D_1^+} = \mathbf{N}_k^1|_{\partial D_1^-}, \quad k = 1, 2, 3, \quad (17)$$

and

$$\begin{aligned} & \left[ (k_r + \mu_{Tr}) \mathbf{N}_{1,1}^r + (k_r - \mu_{Tr}) \mathbf{N}_{2,2}^r \right]_+^+ n_1 \\ & + \left[ \mu_{Tr} (\mathbf{N}_{1,2}^r + \mathbf{N}_{2,1}^r) \right]_+^+ n_2 = \mathbf{A} n_1 + \mathbf{C} n_2, \end{aligned} \quad (18)$$

$$\begin{aligned} & \left[ (k_r + \mu_{Tr}) \mathbf{N}_{2,2}^r + (k_r - \mu_{Tr}) \mathbf{N}_{1,1}^r \right]_+^+ n_2 \\ & + \left[ \mu_{Tr} (\mathbf{N}_{1,2}^r + \mathbf{N}_{2,1}^r) \right]_+^+ n_1 = \mathbf{C} n_1 + \mathbf{B} n_2, \end{aligned} \quad (19)$$

$$[\mu_{Ar} \mathbf{N}_{3,\alpha}^r]_+^+ n_\alpha = \mathbf{D}_\alpha n_\alpha, \quad (20)$$

where the components of  $\mathbf{A}$ ,  $\mathbf{B}$ ,  $\mathbf{C}$  and  $\mathbf{D}_\alpha$  are

$$\begin{aligned} A_{pm} &= (k_1 - k_0) \delta_{pm} + (\mu_1 - \mu_{T0}) \\ & \times (2\delta_{1p}\delta_{1m} - \delta_{pm}) - \eta_0 \delta_{p3}\delta_{m3}, \end{aligned} \quad (21)$$

$$\begin{aligned} B_{pm} &= (k_1 - k_0) \delta_{pm} + (\mu_1 - \mu_{T0}) \\ & \times (2\delta_{2p}\delta_{2m} - \delta_{pm}) - \eta_0 \delta_{p3}\delta_{m3}, \end{aligned} \quad (22)$$

$$C_{pm} = (\mu_1 - \mu_{T0})(\delta_{1p}\delta_{2m} + \delta_{2p}\delta_{1m}), \quad (23)$$

$$D_{\alpha pm} = (\mu_1 - \mu_{A0})(\delta_{\alpha m}\delta_{3p} + \delta_{\alpha p}\delta_{3m}). \quad (24)$$

where  $\delta_{pm}$  is the Kronecker symbol. We have made use of the isotropy of the pores, so that  $\mu_{T1} = \mu_{A1} = \mu_1$ . We note that the difference in cell problems is due to the additional term in (21), (22) which modifies the  $(p, m) = (3, 3)$  cell problem. Note that the cell problem for  $\mathbf{N}_3$  is decoupled from that of  $\mathbf{N}_1$  and  $\mathbf{N}_2$ . The former is associated with *anti-plane* motion whereas the latter is associated with *in-plane* motion.

### 3.1 The homogenized wave equation

The  $O(\epsilon^2)$  problem is used to determine the effective wave equation governing the leading order displacement  $U_k(\mathbf{z})$ . This is achieved by integrating the governing equation at  $O(\epsilon^2)$  over the periodic cell, employing the divergence theorem and imposing the necessary boundary conditions and (hexagonal) double-periodicity in  $\xi$ . Restricting attention to circular pores, this gives rise to the effective wave equations (Parnell and Abrahams 2006, 2008)

$$C_{ijkl}^* U_{j,kl} + d_* U_i = 0, \quad (25)$$

where  $U_{k,j}$  denotes the derivative of  $U_k$  with respect to  $z_j$ ,  $C_{ijkl}^*$  is the effective *transversely isotropic* elastic modulus tensor, and  $d_* = (1 - \phi) + \phi(\rho_1/\rho_0)$  is the effective density,

scaled on  $\rho_0$ . The form of the components of  $C_{ijkl}^*$  will be given shortly.

From hereon in it is more convenient to work with the Voigt notation for the elastic coefficients [see e.g. [Sokolnikoff \(1956\)](#)] rather than the tensorial notation. We note the relations

$$c_{11}^* = C_{1111}^*, \quad c_{33}^* = C_{3333}^*, \quad c_{44}^* = C_{1313}^*, \quad (26)$$

$$c_{12}^* = C_{1122}^*, \quad c_{13}^* = C_{1133}^*, \quad c_{66}^* = C_{1212}^*, \quad (27)$$

and (5)–(9) noting that  $c_{66}^* = \frac{1}{2}(c_{11}^* - c_{12}^*)$  for transverse isotropy. In order to completely define all five independent effective elastic moduli, we require the solution to the cell problem associated with only *three* of the forcings in the boundary conditions above. These are the in-plane problems with  $p = m = 1$  and  $p = m = 3$  and also the anti-plane problem with  $p = 3$  and  $m = 1$ .

The five effective properties are defined as

$$k^* = k^{*A} + (k_1 - k_0 + \mu_1 - \mu_{T0})(M_1 + M_2), \quad (28)$$

$$\mu_T^* = \mu_T^{*A} + (\mu_1 - \mu_{T0})(M_1 - M_2), \quad (29)$$

$$\ell^* = k^{*A} + \mu_T^{*A} + (k_1 - \mu_1 - \ell_0)(M_1 + M_2) \quad (30)$$

$$\gamma^* = (1 - \phi)\gamma_0 + \phi(k_1 + \mu_1) + (k_1 - \mu_1 - \ell_0)M_3 \quad (31)$$

$$\mu_A^* = \mu_A^{*A} + (\mu_1 - \mu_{A0})M_4 \quad (32)$$

where the superscript  $*A$  denotes the arithmetic mean, e.g.  $k^{*A} = (1 - \phi)k_0 + \phi k_1$ , and we note that  $c_{11}^* = k^* + \mu_T^*$ ,  $c_{12}^* = k^* - \mu_T^*$ ,  $c_{13}^* = \ell^*$ ,  $c_{33}^* = \gamma^*$  and  $c_{44}^* = \mu_A^*$ . Also  $\phi = |D_1|/|D| = \pi R^2/|D|$  is the mesoscopic porosity of the bone (i.e. the porosity of the local region of interest) or alternatively, in the language of composite materials, the volume fraction of the pore phase. In the definition of  $\phi$ ,  $R$  is the radius of circular pores. The coefficients  $M_j$  are determined by line integrals of  $N_k^{pm}$  around the cylindrical pore boundary  $\partial D_1$

$$M_1 = \frac{1}{|D|} \int_0^{2\pi} N_1^{11}(\theta) n_1(\theta) \, d\theta, \quad (33)$$

$$M_2 = \frac{1}{|D|} \int_0^{2\pi} N_2^{11}(\theta) n_2(\theta) \, d\theta, \quad (34)$$

$$M_3 = \frac{1}{|D|} \int_0^{2\pi} (N_1^{33}(\theta) n_1(\theta) + N_2^{33}(\theta) n_2(\theta)) \, d\theta, \quad (35)$$

$$M_4 = \frac{1}{|D|} \int_0^{2\pi} N_3^{31}(\theta) n_1(\theta) \, d\theta, \quad (36)$$

where firstly we recall the notation  $N_k^{pm}$  for the  $(p, m)$  cell problem defined in (14), and we note that the local polar coordinate system  $\xi_1 = r \cos \theta$  and  $\xi_2 = r \sin \theta$  (where  $r$  and  $\theta$  are the radial and angular coordinates respectively)

centred on the pore within the periodic cell has been introduced. Finally  $\mathbf{n} = (n_1, n_2)$  is the unit normal to the pore boundary, and thus since here this boundary is circular, we have  $n_1 = \cos \theta$  and  $n_2 = \sin \theta$ .

### 3.2 The solution to the cell problem

The cell problems for isotropic phases were solved in [Parnell and Abrahams \(2006, 2008\)](#). For TI phases, the cell problems are mathematically equivalent, and therefore, we can use the methods developed in those papers. The methods used are based on complex variable theory and multipole expansions of doubly periodic functions, specially constructed to enable complex mesostructure or microstructure to be modelled.

It is unnecessary to give details here. We merely note that the Eqs. (15), (16) are solved subject to the boundary conditions (18)–(20) by posing local expansions in the pore and matrix. These expansions are then matched to doubly periodic functions in order to satisfy double periodicity in  $\xi$ . This process gives a linear system, which is solved for the complex vectors  $\mathbf{a}_1, \mathbf{a}_2, \mathbf{a}_3, \dots, \mathbf{b}_1, \mathbf{b}_2, \mathbf{b}_3, \dots$  for the in-plane problem and real vectors  $\mathbf{c}_1, \mathbf{c}_2, \mathbf{c}_3, \dots$  for the anti-plane problem. The bold fonts indicate the dependence on the  $(p, m)$  cell problem. The local expansion on the boundary  $\partial D_1$  of a *circular* pore of radius  $R$  then takes the form

$$\mathbf{N}_1 = \frac{R}{2\mu_1} \left[ ((\mathcal{K}_1 - 1)\Re(\mathbf{b}_1) - \Re(\mathbf{b}_1) - 3R^2\Re(\mathbf{a}_3)) \cos \theta + (-(\mathcal{K}_1 + 1)\Im(\mathbf{a}_1) + \Im(\mathbf{b}_1) + 3R^2\Im(\mathbf{a}_3)) \sin \theta + \dots \right], \quad (37)$$

$$\mathbf{N}_2 = \frac{R}{2\mu_1} \left[ ((\mathcal{K}_1 + 1)\Im(\mathbf{a}_1) + \Im(\mathbf{b}_1) + 3R^2\Im(\mathbf{a}_3)) \cos \theta + ((\mathcal{K}_1 - 1)\Re(\mathbf{a}_1) + \Re(\mathbf{b}_1) + 3R^2\Re(\mathbf{a}_3)) \sin \theta + \dots \right], \quad (38)$$

$$\mathbf{N}_3 = \mathbf{c}_1 R \cos \theta + \dots \quad (39)$$

where  $\Re$  and  $\Im$  define the real and imaginary parts respectively and where we have defined  $\mathcal{K}_1 = (k_1 + 2\mu_1)/k_1$ . These solutions are then used in (33)–(36) and then (28)–(32) in order to determine the effective properties. The additional terms denoted by  $+\dots$  in (37) and (38) are higher order terms associated with  $\cos n\theta$  and  $\sin n\theta$  but we see from the form of (33), (34) that these do not contribute to the expressions for the effective moduli due to orthogonality (this is only the case for *circular* cylindrical pores). Programs to solve these problems and thus find the necessary coefficients in  $\mathbf{N}_1, \mathbf{N}_2$  and  $\mathbf{N}_3$  above were written by the authors in Mathematica software. This package permits very simple and concise algorithms to be implemented and used. Additionally the authors have also recently created a code with MATLAB software that implements the above model ([Grimal and Parnell 2011](#)).

**Table 1** We refer to the following (dimensional, i.e. with hats, in GPa) isotropic Zysset et al. (1999) and transversely isotropic Hofmann et al. (2006) stiffness values for the bone matrix

	$\hat{c}_{11}^0$	$\hat{c}_{33}^0$	$\hat{c}_{12}^0$	$\hat{c}_{13}^0$	$\hat{c}_{44}^0$	$\hat{c}_{66}^0$
Iso	30.28	30.28	12.98	12.98	8.65	8.65
TI	30.62	34.28	12.62	12.97	10.40	9.00

#### 4 Models for the elastic behaviour cortical bone

Various assumptions have been made regarding the pore properties of cortical bone. Here we consider *hard* and *soft* pores. Hard indicates that cylindrical pores are filled with water at rest. The properties of inviscid water are described by its bulk modulus  $\hat{K}_1 = 2.2$  GPa and shear modulus  $\hat{\mu}_1 = 0$ ; Soft indicates that the limiting case of a void (cavity) is taken with the values  $\hat{K}_1$  and  $\hat{\mu}_1$  tending towards zero. Note that we used “hats” to denote dimensional properties. Also, for computations, we take  $\hat{\mu}_1$  very small rather than identically zero. We could also rewrite the boundary conditions in order to ensure that the inclusion can only accommodate dilatation and not shear. We have confirmed numerically that these two approaches yield identical results, however.

A wide range in variation of cortical bone matrix properties have been quoted in the literature although often data are incomplete since it is difficult to measure all components of the stiffness tensor. In Parnell and Grimal (2009), the matrix was considered isotropic. Here we assume a *transversely isotropic* matrix with properties as given in Hofmann et al. (2006) who used a combination of acoustic microscopy and nanoindentation to find transverse and axial Young’s moduli in the osteon lamellae as  $\hat{E}_{T0} = 23.4$  GPa,  $\hat{E}_{A0} = 26.5$  GPa. The axial shear modulus was determined as  $\hat{\mu}_{A0} = 10.4$  GPa. Using the (common) assumption of a Poisson ratio of  $\hat{\nu}_0 = \hat{\nu}_{T0} = \hat{\nu}_{A0} = 0.3$  for all material directions, the corresponding stiffness coefficients are thus derived (via the expressions given in (51)–(53) of Appendix B) and are given in Table 1. These values also correspond to  $\hat{k}_0 = 21.62$  GPa,  $\hat{\mu}_{T0} = 9$  GPa,  $\hat{\gamma}_0 = 34.28$  GPa and  $\hat{\ell}_0 = 12.97$  GPa. When comparing predictions with experimental data later, we allow these matrix properties to vary in order to compensate for matrix property variation which is inevitable.

The predictions as given in this section can be interpreted in two alternative ways. Since the effective moduli are plotted as functions of porosity, this porosity can either be considered as mesoscale or macroscale, thereby permitting the effective properties to be considered as mesoscale properties or macroscale properties. In sections to follow we consider an example of each case by considering first comparisons with experimental data (macroscale) and then by considering models of how the effective properties vary as a function of cross-section of cortical bone due to the porosity gradient.

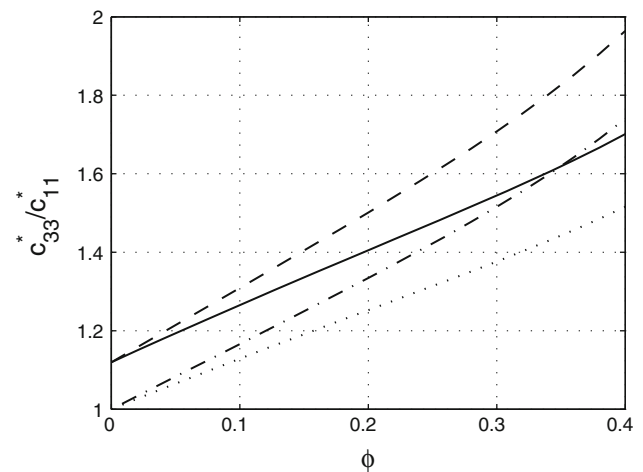


**Fig. 3** The anisotropy ratio  $c_{33}^*/c_{11}^*$  as a function of porosity. We plot results for the considered TI and isotropic matrix properties for hard and soft pores. TI and soft pore (dashed line); TI and hard pore (solid line); isotropic and soft pore (dot-dash line); isotropic and hard pore (dotted line)

##### 4.1 Influence of matrix anisotropy

In Fig. 3 we plot the macroscopic anisotropy ratio (AR), plotted as a function of cortical bone porosity for both isotropic and TI matrix properties as taken from Table 1. We consider both cases of hard and soft pores. We note that the soft pore case increases the AR compared with the hard pore case as was noted in Parnell and Grimal (2009) and as should be expected the additional anisotropy due to the TI matrix phase gives rise to the value typically measured in cortical bone at the usual porosities quoted above, i.e. an AR of around 1.3–1.5.

Various factors play a role in the modification of mechanical properties of cortical bone, which induce a variation of the macroscopic AR through a coupled process of bone resorption and formation called bone remodelling. Amongst the various factors playing an important role in the level of turnover of bone, we have in particular, nutrition, drug exposure and physical exercise. These factors can also change the contribution to the AR in specific ways; for example, drugs can independently affect porosity or matrix anisotropy. This study, where both porosity and anisotropy are also studied independently, can therefore be used in this context in order to assess their relative contribution to macroscopic AR.

##### 4.2 Comparison of popularly used analytical schemes

Variational methods place bounds on engineering constants (Young’s moduli, Poisson ratios, etc.) rather than components of the elastic modulus tensor and so we plot predictions of the engineering constants when comparing various analytical methods. Relationships between elastic moduli and

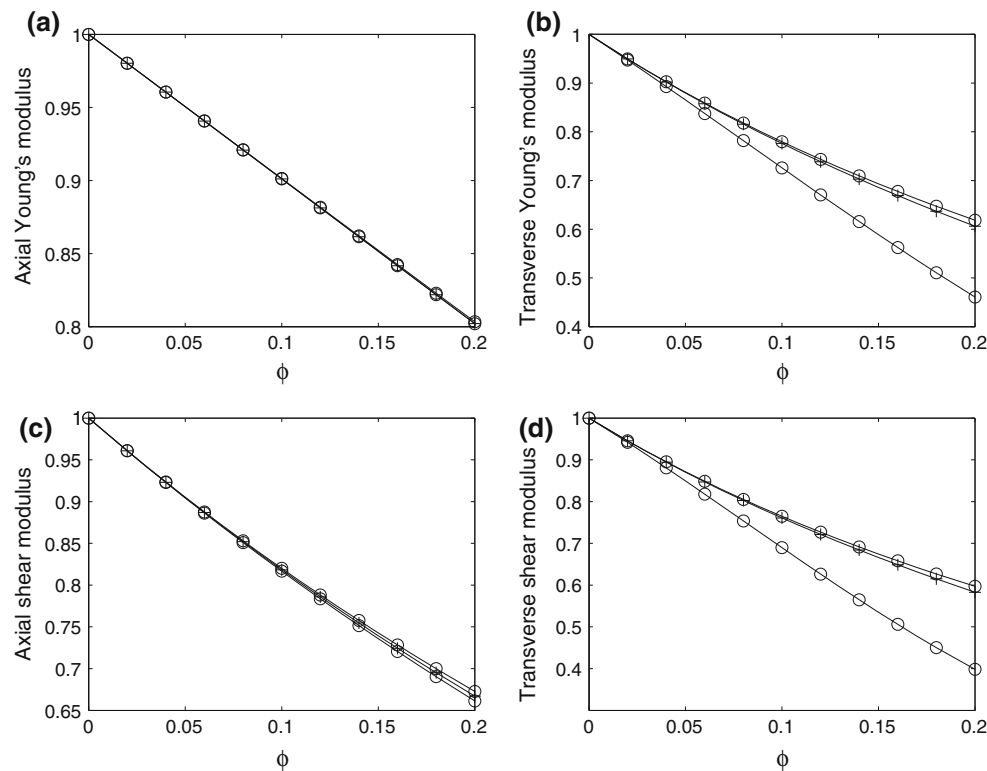


**Fig. 4** Case of hard pores. Engineering moduli plotted as a function of  $\phi$ . **a** Axial Young's modulus; **b** Transverse Young's modulus; **c** axial shear; **d** transverse shear. All results are normalized on their corresponding matrix property so that they are unity when  $\phi = 0$ . In each graph

here, four curves are plotted: + for asymptotic method; o for Hashin–Rosen bounds. MT method is almost indistinguishable from the MAH in this case, and therefore, it is considered more clearly in Fig. 6 by different means

engineering constants for TI materials are given in (49)–(50) of Appendix B. Here we employ the Hashin–Rosen (HR) variational bounds on the effective elastic properties of periodic inhomogeneous media (see Appendix D.2). These appear to be less well known than the corresponding Hashin–Shtrikman (HS) bounds on random media. Since here we model bone as periodic, the predicted properties via the MAH must sit inside the HR bounds. In addition to the MAH, we also consider the Mori–Tanaka (MT) approach (described briefly in Appendix C). Note that the MT method does *not* have to sit inside the HR bounds since its predictions refer to random media.

In Figs. 4, 5 and 6 we present results associated with hard pores whereas Fig. 7 concerns the case of soft pores. In all results we re-scale the property on its corresponding matrix value so that the normalized plots for the effective moduli in Figs. 4, 5 and 7 give an effective modulus which takes the value of unity when  $\phi = 0$ .

#### Hard pores

In all cases the MAH and MT schemes are very close in the volume fraction ranges of relevance to cortical bone. The largest deviation between these two schemes is with  $\nu_A^*$ . In

all cases except for  $\nu_A^*$  the MT method predictions sit inside the HR bounds in the volume fraction range considered. In fact for this modulus we also plot the Hashin–Shtrikman (HS) bounds, and we see that the MT prediction comfortably sits inside these wider bounds. Figure 5a shows the advantage of the HR bounds over the HS bounds if we know that the material is periodic. The MAH sits inside the HR bounds in the ranges of volume fraction considered and can in fact be shown to sit inside for all  $\phi$  up to its filling fraction. The Hashin–Rosen bounds are very tight for axial properties but less tight for transverse properties, especially the transverse Poisson ratio so that it seems the micromechanical predictions such as the asymptotic scheme and Mori–Tanaka method, therefore, can have some importance in this scenario in particular. The effective axial Young's modulus has the usual linear dependence on volume fraction. Transverse Young's modulus and shear modulus remain close to the upper HR bound whereas the transverse Poisson ratio stays close to the lower bound.

We stress that in the case of axial properties (axial Young's modulus, shear modulus and Poisson ratio) HR bounds can be of great value in the prediction of effective elastic properties since they are so tight. In Fig. 6 we show a different presentation of these results which allows one to see how



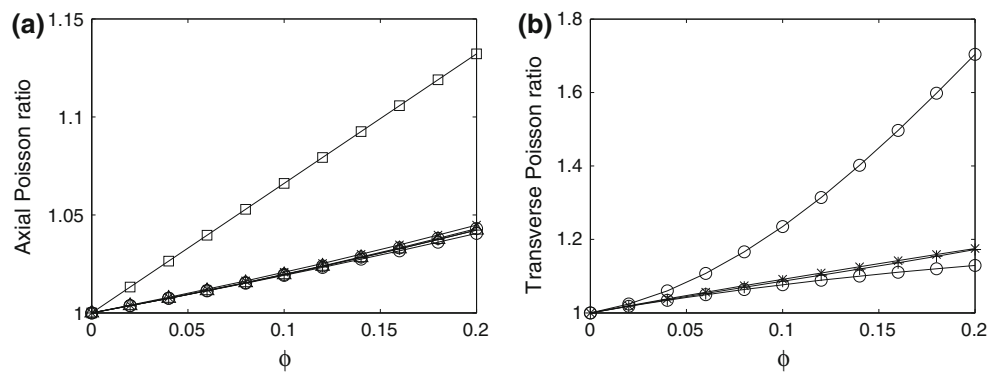


**Fig. 5** Case of hard pores. Effective Poisson ratios plotted as a function of  $\phi$ . **a** Axial; **b** transverse. The symbol of  $\times$  is associated with the MT method. See caption Fig. 4 for other keys. Hashin–Shtrikman bounds are also plotted in **a** here because the MT method lies outside

the HR bounds in this case: *triangle* for lower bound and *square* for upper bound. All results are normalized on their corresponding matrix property so that they are unity when  $\phi = 0$

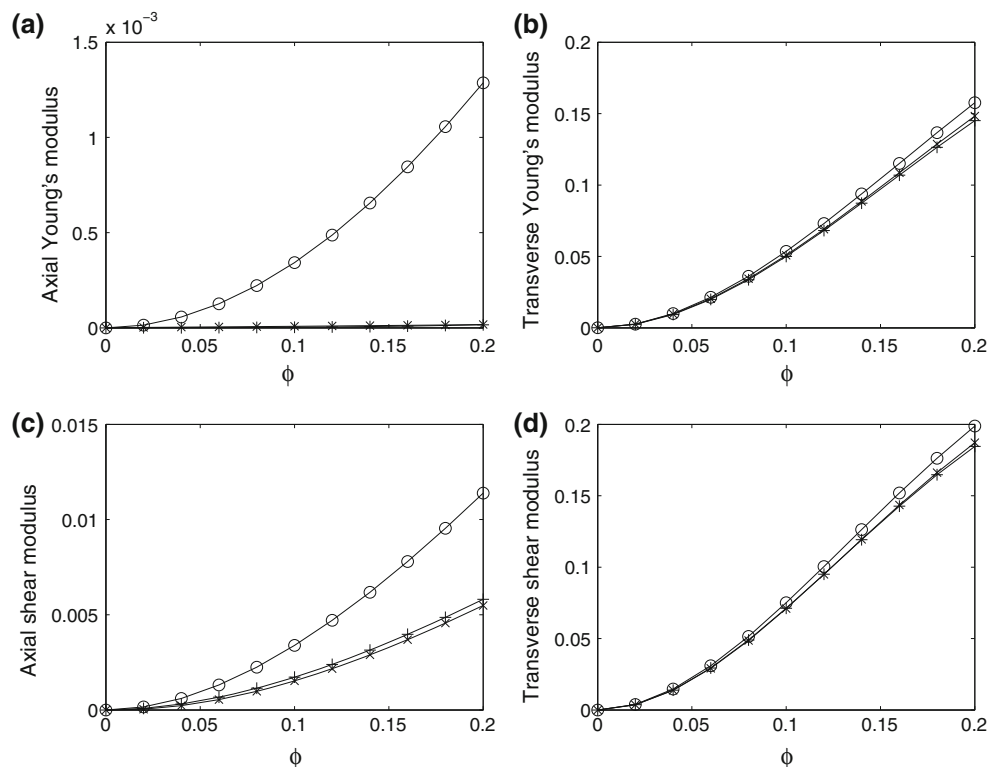


**Fig. 6** Case of hard pores. Engineering moduli plotted as a function of  $\phi$ . In each graph, three curves are plotted. For instance, in **a**, the three quantities are:  $+$  for  $(E_A^* - E_{A(-)})$ ,  $\times$  for  $(E_A^{MT} - E_{A(-)})$  and  $\circ$  for

$(E_{A(+)} - E_{A(-)})$  each of which has been rescaled on the matrix Axial Young's modulus  $\hat{E}_{A0}$ . The same symbols are used in the graphs **b**, **c** and **d** for the other Engineering moduli

close to the bounds such predictions are. For instance, in Fig. 6a, the three curves plotted represent the three quantities  $(E_A^* - E_{A(-)})$ ,  $(E_A^{MT} - E_{A(-)})$  and  $(E_{A(+)} - E_{A(-)})$ , (where  $E_A^{MT}$  denotes the axial Young's modulus predicted by the Mori–Tanaka scheme), but rescaled on the matrix Young's modulus  $\hat{E}_{A0}$ . Thus the scale itself on the vertical axis exhibits how close the bounds are and thus where such micromechanical schemes sit within such bounds. We see in particular

how tight the bounds on the axial properties are compared with their transverse counterparts.

#### Soft pores

In the case of soft pores (cavities), we see from (90) and (91) in Appendix D.4 that there are exact expressions for the axial Young's modulus and Poisson ratio, which are simply

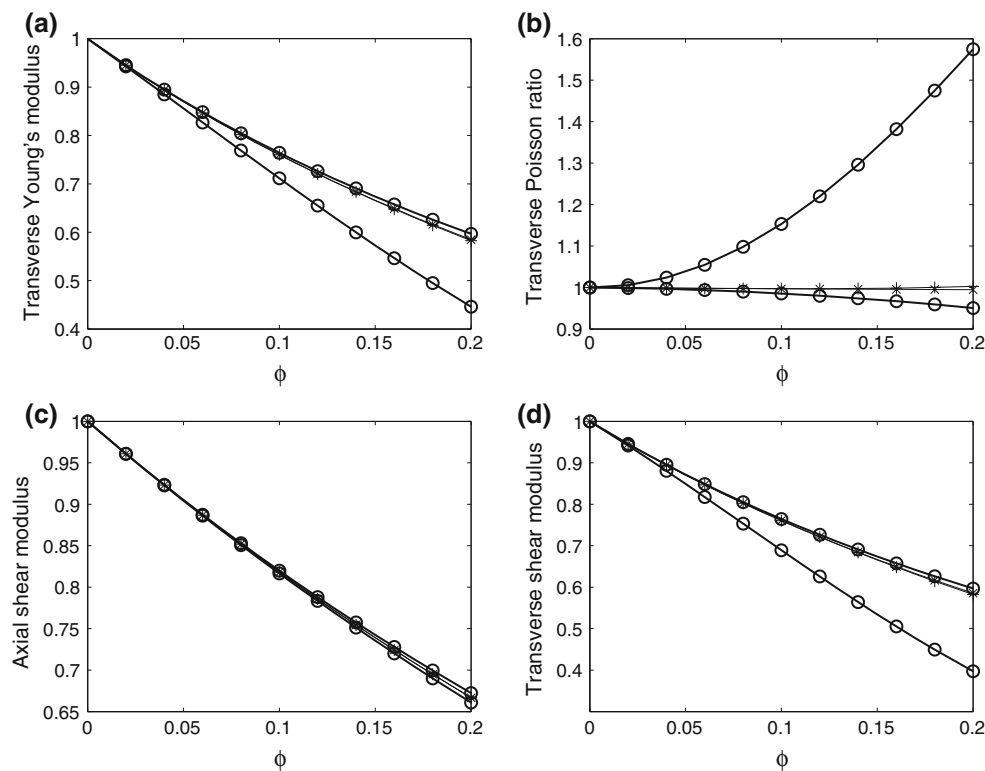


**Fig. 7** Case of soft pores. Engineering moduli plotted as a function of  $\phi$ . **a** Transverse Young's modulus; **b** transverse Poisson ratio; **c** axial shear; **d** transverse shear. All results are normalized on their

corresponding matrix property so that they are unity when  $\phi = 0$ . In each graph, four curves are plotted: + for asymptotic method;  $\times$  for Mori–Tanaka method;  $\circ$  for Hashin–Rosen bounds

$E_A^* = (1 - \phi)E_{A0}$  (once again the typical linear dependence on volume fraction is evident) and  $\nu_A^* = \nu_{A0}$ , simply that of the matrix medium. We do not plot these results. We note in particular that the results for  $\mu_A^*$ ,  $\mu_T^*$  and  $E_T^*$  are almost identical to the hard pore case. The main difference between the two cases is embedded in the Poisson ratios  $\nu_T^*$  and  $\nu_A^*$ . In the case of  $\nu_T^*$ , the HR bounds are not tight, and therefore, the predictive schemes such as the MAH and MT can be of great use in this context. We see in Fig. 7 that for the soft pore case, the MAH prediction for  $\nu_T^*$  is almost constant (unity, corresponding to a physical, dimensional prediction of that of the matrix phase), and therefore, a reasonable approximation is to conclude that both Poisson ratios can be estimated as those of the matrix properties for the case of soft pores. Deviations of the results for the soft pore case (as displayed in Fig. 6 for the hard pore case) follow more or less the same qualitative trend as the hard pore case, except for the Axial Poisson ratio where all methods agree exceptionally well.

## 5 Comparison with experimental data

In the previous section we hypothesized that the MAH is a potentially valuable homogenization method by which one

can predict the effective elastic properties of cortical bone. It is therefore important to compare the predictions of the method with experimental data. It is difficult to obtain complete, reliable experimental data but if it can be found, it almost always corresponds to *macroscopic* tests where the mesodomain is the size of the cortical bone cross-section, and therefore, all information regarding the microscale and mesoscale (porosity gradient for example) has been homogenized.

Figures 8 and 9 concern the cases of both hard and soft pores. We plot each component of the elastic modulus tensor using the MAH with TI matrix properties as defined in Table 1. In addition, the dashed curves above and below this prediction correspond to increasing and decreasing, respectively, the matrix properties by 10%. This deviation permits variation in the matrix properties within the physiological range normally considered [see for example the work of Grimal et al. (2008)]. This accounts for the fact that matrix properties vary significantly between individuals and with age for example. Note that the difference between hard and soft pores is insignificant in the case of  $c_{44}^*$ , and we therefore cannot distinguish between these two cases in Fig. 9.

We compare predictions with two experimental data sets given by Yoon and Katz (1976b) and Rho (1996).

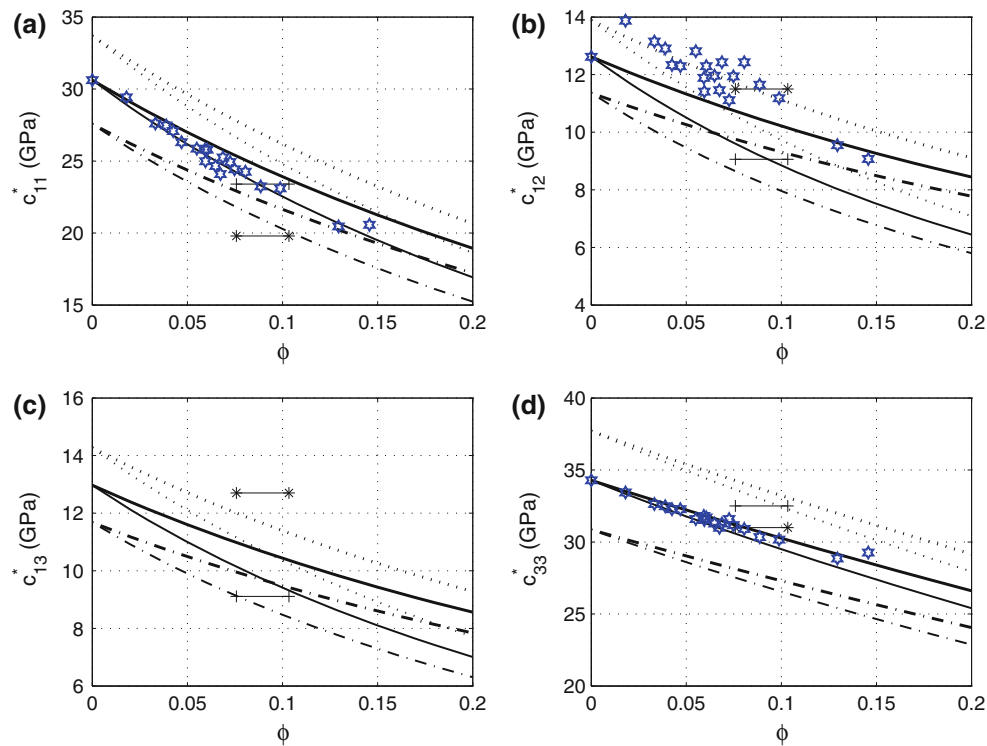


**Fig. 8** Cases of hard and soft pores. The variation of the components of the elastic tensor as a function of  $\phi$  is plotted. The *thick* and *thin* lines are respectively associated with the cases of hard and soft pores. The *solid* lines are obtained by using the values of the components of the elastic tensor given in Table 1 for the bone matrix. *Dotted* and *discontinuous* lines are obtained in increasing and decreasing of 10% the values

of the components of the elastic tensor associated with the bone matrix. The *symbols* of defined *plus* and *star* are respectively associated with experiment measures of Yoon and Katz (1976b) (dry bone) and Rho (1996) (wet bone). The *symbol* of defined *star open* is associated with results of Baron et al. (2007). **a**  $c_{11}^*$  versus  $\phi$ ; **b**  $c_{12}^*$  versus  $\phi$ ; **c**  $c_{13}^*$  versus  $\phi$ ; **d**  $c_{33}^*$  versus  $\phi$

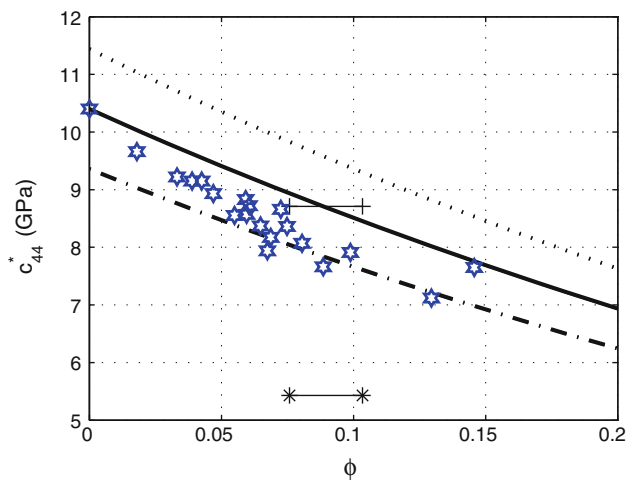


**Fig. 9** Cases of hard and soft pores. See caption of Fig. 8 for key.  $c_{44}^*$  versus  $\phi$ . Note that the difference between hard and soft pores is insignificant in the case of  $c_{44}^*$  and we therefore cannot distinguish between these two cases on the plot

Unfortunately, in these studies, the macroscopic porosity of the test specimens was not measured. This is almost always the case in experimental results regarding the effective elastic

properties of bone. Via ultrasonic techniques, Yoon and Katz (1976b) measured elastic properties on dry bone specimens taken from the human femur. Ultrasonic techniques were used by Rho (1996) to measure the elastic properties of wet human tibia.

The distribution of porosity in specimens of human femoral bone has been studied by Bousson et al. (2001). The mean cortical porosity was 8.26 and 9.72% in males and females respectively. The standard errors of the mean are, respectively, by  $\pm 0.68\%$  and  $\pm 0.62\%$ , which are used to calculate confidence intervals for the means. Using these results, the typical range of porosity in humans is [7.7, 10.32]%. This result is combined with those of Yoon and Katz (1976b) and Rho (1996) in order to draw the corresponding horizontal lines on Figs. 8 and 9.

Because the experiments described in Yoon and Katz (1976b) and Rho (1996) correspond to dry and wet bone respectively, we may hypothesize that the soft and hard pore predictions (respectively) should agree best. In fact as can be seen from the figures, qualitatively (Yoon and Katz 1976b) appears to give better agreement in both cases. It is not entirely clear why this is the case, but is almost certainly associated with the uncertainty in matrix properties

(mineralization). Another possibility for the wet case is that the matrix properties were significantly affected by the presence of water and therefore are very different from those considered above. Excellent agreement with the case of dry bone for soft pores is, however, very encouraging.

It is evident that there are many difficulties associated with comparing predictive schemes with experimental data sets, those being

1. Is it effective or useful to consider a *macroscopic* effective modulus tensor for cortical bone when there is clear variation of the porosity on the mesoscale? In this sense, we could question the validity or usefulness of both experimental and predictive schemes at this scale.
2. Many intricate wave propagation experiments on bone [i.e. the axial transmission technique [Lowet and van der Perre \(1996\)](#), [Bossy et al. \(2004\)](#)] require knowledge of the variation of effective elastic modulus tensor with distance away from the cortical bone surface.
3. Measurement of matrix properties in samples is extremely difficult, in particular, because such properties can vary (as with porosity) with spatial location and specifically with distance along the cortical bone cross-section. Hence predictive schemes are at the mercy of such matrix property predictions.

In the case of point 1. it would seem appropriate to consider the mesoscale rather than macroscale models of cortical bone and therefore move to a mesoscopic homogenization approach. Clearly experimental results at the macroscale are still “meaningful” in some sense but must be interpreted correctly. In particular, along with macroscopic experimental data, it would be of great use if porosity and matrix properties are also determined. Point 2 is directly related to point 1: a mesoscopic model would incorporate such variation. We shall discuss these aspects further in the next section. Regarding point 3, an alternative to matrix property predictions via experiments is to model matrix properties mathematically, once again using homogenization techniques ([Hellmich et al. 2004](#)). However even in these models we are still at the mercy of some experimentally determined data or on assumptions made regarding phase properties. This is always the difficulty with such multiscale approaches, i.e., at which scale do we begin the upscaling process?

To complete this subsection and again with the aim of assessing the validity of the results obtained with the present method, we compare results with those given in [Baron et al. \(2007\)](#). In that work, the authors use numerical simulations coupled with real experimental data of cortical bone microstructure to investigate the effect of porosity on the effective diagonal stiffness coefficients of cortical bone. Bone microstructure geometry was reconstructed from three-dimensional high-resolution synchrotron radiation microcomputed

tomography data sets. The effective properties were obtained by simulating longitudinal and shear wave propagation in three orthogonal directions of the virtual sample. Hence the data account for the effect of the complex shape of pores on the anisotropic elastic properties. Furthermore, the elastic properties of the transversely isotropic matrix were the same for all samples which simplifies the comparison with our model. More precisely, [Baron et al. \(2007\)](#) assumed that pores are filled with inviscid water and the elastic properties of the matrix [model 2 defined in [Baron et al. \(2007\)](#)] were defined by the transverse and axial Young’s moduli as  $\hat{E}_{T0} = 23.6$  GPa and  $\hat{E}_{A0} = 26.6$  GPa, respectively; the axial shear modulus was defined as  $\hat{\mu}_{A0} = 10.4$  GPa. Poisson ratios were defined as  $\hat{\nu}_0 = \hat{\nu}_{T0} = \hat{\nu}_{A0} = 0.3$  for all material directions. These matrix properties are sufficiently close to those used for the TI matrix in the present work to be directly compared with our results and thus the data from [Baron et al. \(2007\)](#) is plotted in Figs. 8 and 9 (using the symbol  $\clubsuit$ ). It is evident that there is good agreement with our results except in the case of  $c_{12}^*$ . We note however that this modulus is not obtained directly by the numerical simulation but via (53).

## 6 Variation of effective moduli with cross-section

The predictive schemes of homogenization and micromechanical methods can be interpreted in two alternative ways, depending upon the choice of mesodomain size.

1. Choosing the mesodomain as the size of the cortical bone cross-section (i.e. the macroscale), the porosity is then defined as the porosity of that whole sample. Thus the macroscopic effective moduli are predicted as a function of this macroscopic porosity,
2. Choosing the mesodomain at the mesoscale, i.e. at a scale above the microscale but below the macroscale, permits the prediction of effective properties *which vary as a function of porosity across the cortical bone cross-section*.

The choice of 1. or 2. above depends on the need for determining and subsequent use of the resulting effective moduli. Published experimental data almost always relate to case 1. since tests (e.g. ultrasound) are carried out on macroscopic samples and wavelengths are always much larger than the cross-section of cortical bone.

Here we discuss the fact that the use of 2. above permits us to capture the variation of effective elastic moduli of bone with porosity which varies across the cortical bone thickness. This variation in porosity is heterogeneous at all ages and for both genders ([Bousson et al. 2001](#); [Thomas et al. 2005](#)): the mean porosity in the endosteal region (inner part of

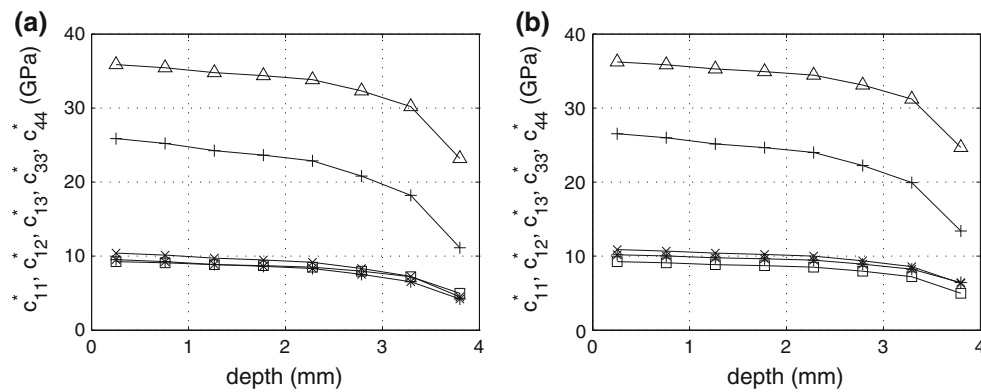


**Fig. 10** Variations of  $c_{11}^*$  (square),  $c_{33}^*$  (plus),  $c_{12}^*$  (star),  $c_{13}^*$  (multiple), and  $c_{44}^*$  (triangle) as a function of the depth. **a** Case of soft pores. **b** Case of hard pores

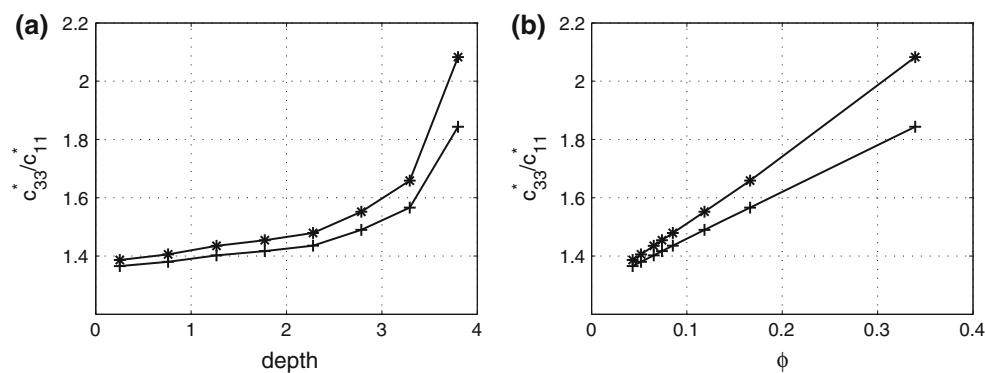


**Fig. 11** The anisotropy parameter  $c_{33}^*/c_{11}^*$  as a function of porosity. The symbols star and plus are respectively associated with the cases of soft and hard pores

the bone) is significantly higher than in the periosteal region (outer part of the bone). Moreover, cortical bone is affected by age-related bone resorption and osteoporosis. It undergoes a thinning of the cortical shell, as well as an increase in porosity, mainly from the endosteal region (Bousson et al. 2001). Therefore, porosity in the radial direction may become more heterogeneous with ageing and/or osteoporosis. An increase in porosity is likely to affect bone material properties (mass density and elasticity), which may, in turn, impact bone quality. Similarly, a thinning of the cortical shell is an important indicator of decreasing bone strength and of fracture risk (Turner 2002).

In a recent paper (Sansalone et al. 2010) carried out experiments on a specimen of human femoral cortical bone from a 79-year old patient to estimate the average variation of porosity and bone mineral density along the bone radial and axial position via a 3D-image processing method. Each 2D-image, corresponding to the cross-sections in the plane  $(x_1, x_2)$ , was analyzed identifying regions of interest going from the periosteum to the endosteum. In this section, average values of porosity as a function of depth (from the periosteum to the endosteum) will be used as input parameters in the

asymptotic homogenization model described in Sect. 3 to compute the local average elastic properties of the bone.

Figures 10a and b concern the cases of hard and soft pores respectively. In each case, the variations of  $c_{11}^*$ ,  $c_{12}^*$ ,  $c_{13}^*$ ,  $c_{33}^*$  and  $c_{44}^*$  are given as a function of depth in the cross-section of the cortical bone.

The standard parameter studied in order to assess the change in anisotropy for transversely isotropic materials is the anisotropy ratio (AR)  $c_{33}^*/c_{11}^*$ . Figure 11 shows the variation of the AR as a function of depth. In particular we note that the AR for bone is typically quoted at around 1.5 (on macroscopic samples). The mesoscopic predictions show that the local (mesoscopic) AR has the potential to deviate significantly from this macroscopic value due to the porosity variation.

## 7 Conclusions

In this paper we have used a variety of micromechanical models in order to consider both macro- and mesoscale elastic behaviour of cortical bone under the assumption of a TI



matrix phase and circular cylindrical pores. In particular we have introduced a scheme based on asymptotic homogenization and a novel solution to the associated cell problem. This scheme can be useful for parametric studies associated with cortical bone and the associated code “bonhomme” is freely available (Grimal and Parnell 2011). Although complex geometries, available via imaging, can now be studied using advanced computational methods, it is often difficult to interpret results from such studies.

The additional influence on the (macroscopic) anisotropy ratio (AR) from the intrinsic anisotropy of the bone matrix (in addition to anisotropy which arises purely from geometrical effects Parnell and Grimal 2009) and the resulting values were in good agreement with typically quoted values of 1.3–1.5. The present study allows us to compare the relative contribution to anisotropy from these two sources, which is of direct interest practically because medical treatments may alter either of these contributions by differing magnitudes.

By comparing various methods, we showed that, under the assumption of periodic geometry, the Hashin–Rosen bounds can be of great use as a predictive tool, especially for axial engineering moduli where these bounds remain very close for the volume fractions considered.

We compared predictions from asymptotic homogenization using common values for the matrix of cortical bone with experimental results from the literature (with some spread due to uncertainty), the main difficulty in such comparisons being the lack of knowledge of porosity and degree of mineralization associated with the experimental data. Therefore we have to assume that they are in some sense associated with “average” population values with some error. In particular, with the experimental data of Yoon and Katz (1976b), we showed that agreement is excellent for the case of dry bone/soft pores. Agreement was less convincing for wet bone/hard pores which we attributed to a number of factors, mainly associated with variation in matrix properties.

Since there is a well-documented gradient in porosity across the cross-section of cortical bone, we showed that it is possible to use the mesodomain at the mesoscale in order to capture this behaviour and thus to model its effect on the variation in elastic moduli with thickness. We note in particular that the variation of the anisotropy ratio with depth away from the cortical bone cross-section can be quite significant. Because the spatial variations of porosity are related to the quality of the physiological bone turnover, which is affected by the complex 3-D stress distribution, abnormal values of porosity are related to alterations of bone remodelling activity which can have critical effects on bone strength. This motivates a need for incorporating the effect of the porosity variation in predictive schemes and in particular for wave propagation models in cortical bone. It is also clear that age has a significant impact on the effective elastic properties of

bone which motivates the study of the age dependence of effective properties.

Pore shape (Parnell and Grimal 2009; Lydzba and Shao 2000) and local anisotropy due to the lamellae (Hamad et al. 2010; Rohan and Cimrman 2011) could also give rise to additional effects in cortical bone. These are aspects which deserve attention, although as we described above, the numerical simulations in Baron et al. (2007) incorporated the complex pore shapes, and the averaging effect over orientation clearly results in predictions that are close to those found using micromechanical methods, including the asymptotic scheme. Future work will focus on coherent model/experimental validation using experimental results currently being undertaken and further models including the variation in both porosity and matrix properties across the cross-section of cortical bone. Three-dimensional analogies of this theory could also be implemented in order to model trabecular bone.

**Acknowledgments** Parnell is grateful to Université Paris-Est Créteil for financial support received during the course of this research. Vu would like to thank Université Paris-Est Créteil and the Manchester Institute for Mathematical Sciences (University of Manchester) for financial assistance in support of this work. The authors thank C. Baron for the data provided in Figs. 8 and 9.

## Appendix

### A Transversely isotropic tensors

It is straightforward to write down transversely isotropic (TI) tensors in the following basis tensor form which is originally due to Hill (1963) (Hill considered this basis implicitly, he did not explicitly write down its form)

$$C_{ijkl} = \sum_{n=1}^6 X_n \mathcal{H}_{ijkl}^{(n)}, \quad (40)$$

where

$$\mathcal{H}_{ijkl}^{(1)} = \frac{1}{2} \Theta_{ij} \Theta_{kl}, \quad \mathcal{H}_{ijkl}^{(2)} = \Theta_{ij} \delta_{k3} \delta_{l3}, \quad \mathcal{H}_{ijkl}^{(3)} = \Theta_{kl} \delta_{i3} \delta_{j3}, \quad (41)$$

$$\mathcal{H}_{ijkl}^{(4)} = \delta_{i3} \delta_{j3} \delta_{k3} \delta_{l3}, \quad \mathcal{H}_{ijkl}^{(5)} = \frac{1}{2} (\Theta_{ik} \Theta_{lj} + \Theta_{il} \Theta_{kj} - \Theta_{ij} \Theta_{kl}), \quad (42)$$

$$\mathcal{H}_{ijkl}^{(6)} = \frac{1}{2} (\Theta_{ik} \delta_{l3} \delta_{j3} + \Theta_{il} \delta_{k3} \delta_{j3} + \Theta_{jk} \delta_{l3} \delta_{i3} + \Theta_{jl} \delta_{k3} \delta_{i3}), \quad (43)$$

and where

$$\Theta_{ij} = \delta_{ij} - \delta_{i3} \delta_{j3}. \quad (44)$$

Let us define the shorthand notation

$$\mathcal{H}^{(m)} \mathcal{H}^{(n)} = \mathcal{H}_{ijpq}^{(m)} \mathcal{H}_{pqkl}^{(n)}, \quad (45)$$

for contraction between the basis tensors defined in (41)–(43). The contractions defined in (45) are summarized in Table 2.

**Table 2** The contractions of the basis tensors  $\mathcal{H}_{ijkl}^{(n)}$ 

	$\mathcal{H}^{(1)}$	$\mathcal{H}^{(2)}$	$\mathcal{H}^{(3)}$	$\mathcal{H}^{(4)}$	$\mathcal{H}^{(5)}$	$\mathcal{H}^{(6)}$
$\mathcal{H}^{(1)}$	$\mathcal{H}^{(1)}$	$\mathcal{H}^{(2)}$	0	0	0	0
$\mathcal{H}^{(2)}$	0	0	$2\mathcal{H}^{(1)}$	$\mathcal{H}^{(2)}$	0	0
$\mathcal{H}^{(3)}$	$\mathcal{H}^{(3)}$	$2\mathcal{H}^{(4)}$	0	0	0	0
$\mathcal{H}^{(4)}$	0	0	$\mathcal{H}^{(3)}$	$\mathcal{H}^{(4)}$	0	0
$\mathcal{H}^{(5)}$	0	0	0	0	$\mathcal{H}^{(5)}$	0
$\mathcal{H}^{(6)}$	0	0	0	0	0	$\mathcal{H}^{(6)}$

## B Notation

Given the Voigt or engineering notation of the elastic moduli  $c_{ij}$  introduced in (26), (27), we can define the corresponding components  $s_{ij}$  of the (symmetric) compliance matrix as

$$s_{11} = 1/E_T, \quad s_{33} = 1/E_A, \quad s_{44} = 1/\mu_A, \quad (46)$$

$$s_{12} = -\nu_T/E_T, \quad s_{13} = -\nu_A/E_A, \quad s_{66} = 1/\mu_T. \quad (47)$$

where  $E_{A,T}$  are respectively the Axial (A) and Transverse (T) Young's moduli,  $\nu_{A,T}$  are respectively the Axial (A) and Transverse (T) Poisson's ratios and  $\mu_{A,T}$  are respectively the Axial (A) and Transverse (T) shear moduli. Note also that we use the notation  $\nu_A = \nu_{31}$  which is a measure of the contraction in the transverse direction ( $x_1$ ), given a force in the axial direction ( $x_3$ ). Note that

$$\frac{\nu_{31}}{E_3} = \frac{\nu_A}{E_A} = \frac{\nu_{13}}{E_1} = \frac{\nu_{13}}{E_T}, \quad (48)$$

and since here we have a transversely isotropic material we have  $\nu_T = \nu_{12} = \nu_{21}$ .

By inverting the matrix with components  $s_{ij}$ , we obtain the matrix with components  $c_{ij}$ , and therefore, it is simple to obtain the relations between Engineering moduli and elastic properties

$$E_A = \frac{c_{11}c_{33} - 2c_{13}^2 + c_{33}c_{12}}{c_{11} + c_{12}},$$

$$E_T = \frac{c_{11}^2c_{33} + 2c_{13}^2c_{12} - 2c_{11}c_{13}^2 - c_{33}c_{12}^2}{c_{11}c_{33} - c_{13}^2}, \quad (49)$$

$$\nu_A = \frac{c_{13}}{c_{11} + c_{12}},$$

$$\nu_T = \frac{c_{12}c_{33} - c_{13}^2}{c_{11}c_{33} - c_{13}^2}, \quad \mu_A = c_{55},$$

$$\mu_T = \frac{c_{11} - c_{12}}{2} = \frac{E_T}{2(1 + \nu_T)}, \quad (50)$$

and furthermore, we note that

$$c_{11} = \frac{E_T(E_A - E_T\nu_A^2)}{(1 + \nu_T)(E_A - E_A\nu_T - 2E_T\nu_A^2)},$$

$$c_{12} = \frac{E_T(E_A\nu_T + E_T\nu_A^2)}{(1 + \nu_T)(E_A - E_A\nu_T - 2E_T\nu_A^2)}, \quad (51)$$

$$c_{13} = \frac{E_TE_A\nu_A}{E_A - E_A\nu_T - 2E_T\nu_A^2},$$

$$c_{33} = \frac{E_A^2(1 - \nu_T)}{E_A - E_A\nu_T - 2E_T\nu_A^2}, \quad (52)$$

$$c_{44} = \mu_A,$$

$$c_{66} = \frac{c_{11} - c_{12}}{2} = \frac{E_T}{2(1 + \nu_T)} = \mu_T. \quad (53)$$

## C The Mori–Tanaka micromechanical method

It is straightforward to show by taking volume averages that an expression for the effective elastic tensor of a two-phase particulate composite where the particulate phase has volume fraction  $\phi$  can be written in the form [see e.g. (2.64) on p. 49 of Markov (1999)]

$$C_{ijkl}^* = C_{ijkl}^0 + \phi(C_{ijmn}^1 - C_{ijmn}^0)A_{mnkl}, \quad (54)$$

where  $A_{mnkl}$  is known as the strain concentration tensor of the particulate phase (phase 1) relating the average strain  $\bar{e}_{ij}^1$  over this phase to the overall averaged strain  $\bar{e}_{ij}$ , i.e.

$$\bar{e}_{ij}^1 = A_{ijkl}\bar{e}_{kl}. \quad (55)$$

The key to micromechanical approximations for effective moduli is then how to determine the strain concentration tensor. The Mori–Tanaka scheme proceeds by firstly defining a secondary concentration tensor, relating the averaged strain over the particulate phase to that of the matrix phase  $\bar{e}_{ij}^0$  via the following expression

$$\bar{e}_{ij}^1 = B_{ijkl}\bar{e}_{kl}^0. \quad (56)$$

Using this in the standard equation for total averaged strain, i.e.

$$\bar{e}_{ij} = \phi\bar{e}_{ij}^1 + (1 - \phi)\bar{e}_{ij}^0 = (\phi B_{ijkl} + (1 - \phi)\delta_{ik}\delta_{jl})\bar{e}_{kl}^0, \quad (57)$$

and then substituting into (55) gives

$$\bar{e}_{ij}^1 = A_{ijkl}(\phi B_{klpq} + (1 - \phi)\delta_{kp}\delta_{lq})\bar{e}_{pq}^0. \quad (58)$$

For consistency with (56) we must have

$$B_{ijpq} = A_{ijkl}(\phi B_{klpq} + (1 - \phi)\delta_{kp}\delta_{lq}). \quad (59)$$

A consistent choice for  $B_{ijkl}$  that is valid near  $\phi = 0$  and  $\phi = 1$  is to choose  $B_{ijkl} = A_{ijkl}^{dil}$  where the superscript *dil* denotes the *dilute* strain concentration tensor which is found by solving the so-called single inclusion problem where no

interaction with other inclusions is felt. This tensor is defined via the following

$$B_{ijmn}\tilde{B}_{mnkl} = I_{ijkl}, \quad \tilde{B}_{ijkl} = I_{ijkl} + P_{ijmn}(C_{mnkl}^1 - C_{mnkl}^0), \quad (60)$$

where  $I_{ijkl}$  is the fourth-order identity tensor and  $P_{ijkl}$  is defined via Eshelby's tensor,  $S_{ijkl} = C_{ijmn}^0 P_{mnkl}$ , and we refer the reader to, e.g., Mura (1991) for details of its derivation. For a cylinder in a transversely isotropic material and using the notation (5)–(7) the non-zero components of Eshelby's tensor are [see e.g. Mura (1991)]

$$S_{1111} = S_{2222} = \frac{3k_0 + 2\mu_{T0}}{4(k_0 + \mu_{T0})},$$

$$S_{1122} = S_{2211} = \frac{k_0 - 2\mu_{T0}}{4(k_0 + \mu_{T0})}, \quad S_{3333} = 0, \quad (61)$$

$$S_{1133} = \frac{\ell_0}{2(k_0 + \mu_{T0})},$$

$$S_{3311} = 0, \quad S_{1313} = S_{3131} = S_{3113} = S_{1331} = \frac{1}{4}. \quad (62)$$

It is easily seen that the choice (60) makes the expression (59) valid near both  $\phi = 0$  and  $\phi = 1$  since near  $\phi = 0$  we have  $A_{ijkl} \sim B_{ijkl} = A_{ijkl}^{dil}$  and near  $\phi = 1$  we have  $A_{ijkl} \sim I_{ijkl}$ .

## D Variational bounds for unidirectional composites with transversely isotropic phases

Hashin and Rosen (1964) derived strict bounds on the effective properties of composite materials with periodic microstructure. However, they restricted phases to be isotropic. Bounds on effective properties of periodic materials with transversely isotropic phases can be found in Hashin (1979) who simplified the approach of Hashin and Rosen (1964). Some of the results are not complete, however, being published in a related NASA report. We therefore state them here for completeness.

We use the notation of subscripts  $Tr$  or  $Ar$  for transverse or axial (respectively) properties associated with phase  $r$ . Furthermore note that all of the results stated here are *dimensional*.

### D.1 Composite cylinder assemblage

First, we state some results from the *composite cylinder assemblage* model of fibre-reinforced composites, since the bounds for periodic media are stated most easily in terms of these results. Firstly four of the five properties result in explicit expressions

$$k_c^*(\phi) = k_0 + \frac{\phi}{1/(k_1 - k_0) + (1 - \phi)/(k_0 + \mu_{T0})}, \quad (63)$$

$$E_{Ac}^*(\phi) = (1 - \phi)E_{A0} + \phi E_{A1} + \frac{4(\nu_{A1} - \nu_{A0})^2}{(1/k_1 - 1/k_0)^2} \left( \frac{(1 - \phi)}{k_0} + \frac{\phi}{k_1} - \frac{1}{k_c^*(\phi)} \right), \quad (64)$$

$$\nu_{Ac}^*(\phi) = (1 - \phi)\nu_{A0} + \phi\nu_{A1} - \frac{(\nu_{A1} - \nu_{A0})}{(1/k_1 - 1/k_0)} \times \left( \frac{(1 - \phi)}{k_0} + \frac{\phi}{k_1} - \frac{1}{k_c^*(\phi)} \right), \quad (65)$$

$$\mu_{Ac}^*(\phi) = \mu_{A0} + \frac{\phi}{1/(\mu_{A1} - \mu_{A0}) + (1 - \phi)/(2\mu_{A0})}, \quad (66)$$

and the fifth (the in-plane shear modulus), gives bounds

$$\mu_{Tc(-)}^* \leq \mu_{Tc}^* \leq \mu_{Tc(+)}^*. \quad (67)$$

If  $\mu_{T1} > \mu_{T0}$  and  $k_1 > k_0$

$$\mu_{Tc(-)}^*(\phi) = \mu_{T0} + \frac{\phi\mu_{T0}}{1/(\gamma - 1) + (1 - \phi)/(1 + \beta_0)}, \quad (68)$$

$$\mu_{Tc(+)}^*(\phi) = \mu_{T0} \left[ 1 + \frac{(1 + \beta_0)\phi}{\rho - \phi(1 + 3\beta_0^2(1 - \phi)^2/(\alpha\phi^3 + 1))} \right], \quad (69)$$

where

$$\alpha = \frac{\beta_0 - \gamma\beta_1}{1 + \gamma\beta_1}, \quad \rho = \frac{\gamma + \beta_0}{\gamma - 1},$$

$$\beta_0 = \frac{k_0}{k_0 + 2\mu_{T0}}, \quad \beta_1 = \frac{k_1}{k_1 + 2\mu_{T1}}, \quad \gamma = \frac{\mu_{T1}}{\mu_{T0}}. \quad (70)$$

Alternatively if  $\mu_{T1} < \mu_{T0}$  and  $k_1 < k_0$

$$\mu_{Tc(-)}^*(\phi) = \mu_{T0} \left[ 1 + \frac{(1 + \beta_0)\phi}{\rho - \phi(1 + 3\beta_0^2(1 - \phi)^2/(\alpha\phi^3 - \beta_0))} \right], \quad (71)$$

$$\mu_{Tc(+)}^*(\phi) = \mu_{T0} + \frac{\phi\mu_{T0}}{1/(\gamma - 1) + (1 - \phi)/(1 + \beta_0)}. \quad (72)$$

### D.2 Hashin–Rosen bounds for periodic structures

Define the parameter  $\phi_c$  which is the volume fraction of the largest circle which can be inscribed into the periodic cell in question. Thus for example, for a square this is  $\pi/4$  and for a hexagon it is  $\pi/(2\sqrt{3})$ . Since here we use a *hexagonal* periodic cell,  $\phi_c = \pi/(2\sqrt{3})$  throughout. The bounds on effective properties are now prescribed in terms of the composite cylinder assemblage results (63)–(66) with arguments  $\phi/\phi_c$  as follows [see Hashin and Rosen (1964)]

$$k_{(-)}^*(\phi) = \left( \frac{1 - \phi_c}{k_0} + \frac{\phi_c}{k_c^*(\phi/\phi_c)} \right)^{-1},$$

$$k_{(+)}^*(\phi) = (1 - \phi_c)k_0 + \phi_c k_c^*(\phi/\phi_c), \quad (73)$$

$$\mu_{A(-)}^*(\phi) = \left( \frac{1 - \phi_c}{\mu_{A0}} + \frac{\phi_c}{\mu_{Ac}^*(\phi/\phi_c)} \right)^{-1},$$

$$\mu_{A(+)}^*(\phi) = (1 - \phi_c)\mu_{A0} + \phi_c \mu_{Ac}^*(\phi/\phi_c), \quad (74)$$

$$E_{A(-)}^*(\phi) = (1 - \phi_c)E_0 + \phi_c E_{Ac}^*(\phi/\phi_c),$$

$$E_{A(+)}^*(\phi) = E_{A(-)}^* + \phi_c(1-\phi_c) \frac{4(v_{Ac}^*(\phi/\phi_c) - v_{A0})^2 k_0 k_c^*(\phi/\phi_c)}{k_0(1-\phi_c) + k_c^*(\phi/\phi_c)}. \quad (75)$$

For bounds on the effective axial Poisson ratio  $\nu_A^*$ , define  $P = (v_{A0} - v_{A1})/(k_1 - k_0)$ ,  $Q = (v_{A1}k_1 - v_{A0}k_0)/(k_1 - k_0)$  and

$$\begin{aligned} \nu_a^* &= Q + Pk_0k_1 \left( \frac{1-\phi_c}{k_0} + \frac{\phi_c}{k_c^*(\phi/\phi_c)} \right), \\ \nu_b^* &= Q + Pk_0k_1 \left( \frac{1}{(1-\phi_c)k_0 + \phi_c k_c^*(\phi/\phi_c)} \right). \end{aligned} \quad (76)$$

If  $P < 0$ , we have  $\nu_a^* \leq \nu_A^* \leq \nu_b^*$ , whereas if  $P > 0$  we get  $\nu_b^* \leq \nu_A^* \leq \nu_a^*$ . Note that the corresponding upper and lower bounds of the four effective properties above coincide in the composite cylinder assemblage limit, when  $\phi_c \rightarrow 1$ . This is in contrast to the following bound on the transverse shear modulus, whose bounds do not coincide in this limit. These bounds can be written in the form

$$\begin{aligned} \mu_{T(-)}^*(\phi) &= \left( \frac{1-\phi_c}{\mu_{T0}} + \frac{\phi_c}{\mu_{Tc(-)}^*(\phi/\phi_c)} \right)^{-1}, \\ \mu_{T(+)}^*(\phi) &= (1-\phi_c)\mu_{T0} + \phi_c \mu_{Tc(+)}^*(\phi/\phi_c). \end{aligned} \quad (77)$$

Finally we can also bound  $E_T^*$  via the following expressions

$$\begin{aligned} E_{T(\pm)}^*(\phi) &= \frac{4k_{(\pm)}^*(\phi)\mu_{T(\pm)}^*(\phi)}{k_{(\pm)}^*(\phi) + M_{(\pm)}^*(\phi)\mu_{T(\mp)}^*(\phi)}, \\ M_{(\pm)}^*(\phi) &= 1 + \frac{4k_{(\pm)}^*(\phi)\nu_{A(\mp)}^{*2}(\phi)}{E_{A(\pm)}^*(\phi)}. \end{aligned} \quad (78)$$

Note this last equation is a correction to the corresponding expression on page 546 of Hashin (1979). The bounds on  $\nu_T$  are

$$\nu_{T(\pm)}^*(\phi) = \frac{k_{(\pm)}^*(\phi) - M_{(\pm)}^*(\phi)\mu_{T(\mp)}^*(\phi)}{k_{(\pm)}^*(\phi) + M_{(\pm)}^*(\phi)\mu_{T(\mp)}^*(\phi)}. \quad (79)$$

### D.3 Hashin–Shtrikman bounds for random unidirectional composites

Since the Mori–Tanaka result is derived for a random structure and then for it to be a viable prediction of the effective properties, it must lie inside appropriate bounds, in this case the Hashin–Shtrikman (HS) bounds for unidirectional composites defined by Hashin (1965, 1979). Here we are particularly interested in the bound for  $\nu_A^*$  since the Mori–Tanaka result sits *outside* the Hashin–Rosen bounds for this property. To define the HS bounds on this, however, we need various other results. Let us define the following

$$\mathcal{M}_+ = \max(\mu_{T0}, \mu_{T1}), \quad \mathcal{M}_- = \min(\mu_{T0}, \mu_{T1}), \quad (80)$$

$$\mathcal{K}_+ = \max(k_0, k_1), \quad \mathcal{K}_- = \min(k_0, k_1), \quad (81)$$

and then, the following HS bounds can be defined on the in-plane bulk and shear moduli

$$k_{(\pm)}^* = \left( \frac{k_0(1-\phi)}{k_0 + \mathcal{M}_{\pm}} + \frac{k_1\phi}{k_1 + \mathcal{M}_{\pm}} \right) \left( \frac{(1-\phi)}{k_0 + \mathcal{M}_{\pm}} + \frac{\phi}{k_1 + \mathcal{M}_{\pm}} \right)^{-1} \quad (82)$$

$$\mu_{T(\pm)}^* = \frac{\mathcal{G}_a}{\mathcal{G}_b}, \quad (83)$$

where

$$\mathcal{G}_a = \left( \frac{\mu_{T0}(1-\phi)}{2\mu_{T0}\mathcal{M}_{\pm} + \mathcal{K}_{\pm}(\mu_{T0} + \mathcal{M}_{\pm})} + \frac{\mu_{T1}\phi}{2\mu_{T1}\mathcal{M}_{\pm} + \mathcal{K}_{\pm}(\mu_{T1} + \mathcal{M}_{\pm})} \right), \quad (84)$$

$$\mathcal{G}_b = \left( \frac{(1-\phi)}{2\mu_{T0}\mathcal{M}_{\pm} + \mathcal{K}_{\pm}(\mu_{T0} + \mathcal{M}_{\pm})} + \frac{\phi}{2\mu_{T1}\mathcal{M}_{\pm} + \mathcal{K}_{\pm}(\mu_{T1} + \mathcal{M}_{\pm})} \right). \quad (85)$$

Bounds on the axial Young's modulus are given by

$$E_{A(\pm)}^* = E_{A0}(1-\phi) + E_{A1}\phi - 4P^2k_1^2k_0^2 \left( \frac{1}{k_{(\pm)}^*} - \frac{\phi}{k_1} - \frac{(1-\phi)}{k_0} \right), \quad (86)$$

where we remind the reader that  $P = (v_{A0} - v_{A1})/(k_1 - k_0)$ . On defining

$$\begin{aligned} \nu_c &= v_{A0}(1-\phi) + v_{A1}\phi \\ &\quad + Pk_1k_0 \left( \frac{1}{k_{(-)}^*} - \frac{\phi}{k_1} - \frac{(1-\phi)}{k_0} \right), \end{aligned} \quad (87)$$

$$\begin{aligned} \nu_d &= v_{A0}(1-\phi) + v_{A1}\phi \\ &\quad + Pk_1k_0 \left( \frac{1}{k_{(+)}^*} - \frac{\phi}{k_1} - \frac{(1-\phi)}{k_0} \right), \end{aligned} \quad (88)$$

we have, with  $P < 0$ ,  $\nu_c \leq \nu_A^* \leq \nu_d$  whereas with  $P > 0$  we have

$$\nu_d \leq \nu_A^* \leq \nu_c. \quad (89)$$

Bounds on the transverse properties then follow from using (80), (89) in the expressions (78), (79).

### D.4 Cavity (soft) and water (hard) limits

For a cavity we let pore properties  $k_1$ ,  $E_{A1}$ ,  $E_{T1}$ ,  $\mu_{T1}$ ,  $\mu_{A1}$  tend to zero. This limit is well-defined except in the case of the axial Poisson ratio  $\nu_A^*$  which we note is defined by Hashin (1979) as

$$\nu_A^* = v_{A0}. \quad (90)$$

Furthermore, the expression for axial Young's modulus simplifies significantly to the form

$$E_A^* = (1 - \phi)E_{A0}. \quad (91)$$

One must take care when taking the limits in the in-plane shear modulus bounds above. In particular we have that  $\gamma = \mu_{T1}/\mu_{T0} \rightarrow 0$  for the cavity. The limit of  $\beta_1$  is unclear. However, since everywhere  $\beta_1$  is multiplied by  $\gamma$ , provided  $\mu_{T1}$  and  $k_{T1}$  approach zero at the same rate, then  $\gamma\beta_1 \rightarrow 0$ . Therefore, for the cavity we have

$$\gamma \rightarrow 0, \quad \alpha \rightarrow \beta_0, \quad \rho \rightarrow -\beta_0, \quad (92)$$

and these must therefore be used in the bounds for  $\mu_T^*$ .

For a pore consisting of (inviscid, incompressible) water (isotropic), we take the limit  $\mu_1 = \mu_{T1} = \mu_{A1} \rightarrow 0$  together with  $\nu_1 = \nu_{T1} = \nu_{A1} = 1/2$  in the above results which are all well behaved in this limit.

## References

- Bakhvalov N, Panasenko G (1989) Homogenization: averaging processes in periodic media. Kluwer, Dordrecht
- Baron C, Talmant M, Laugier P (2007) Effect of porosity on effective diagonal stiffness coefficients (cii) and elastic anisotropy of cortical bone at 1 MHz: a finite-difference time domain study. *J Acoust Soc Am* 122(3):1810–1817
- Bossy E, Talmant M, Peyrin F, Akrou L, Cloetens P, Laugier P (2004) An in vitro study of the ultrasonic axial transmission technique at the radius: 1-MHz velocity measurements are sensitive to both mineralization and intracortical porosity. *J Bone Miner Res* 19(9):1548–1556
- Bousson V, Meunier A, Bergot C, Vicaud E, Rocha M, Morais M, Laval-Jeantet A, Laredo J (2001) Distribution of intracortical porosity in human midfemoral cortex by age and gender. *J Bone Miner Res* 16(17):1308–1317
- Cooper D, Thomas C, Clement J, Turinsky A, Sensen C, Hallgrímsson B (2007) Age dependent change in the 3d structure of cortical porosity at the human femoral midshaft. *Bone* 40:957–965
- Cowin S (1999) Bone poroelasticity. *J Biomech* 32:217–238
- Crolet J, Aoubiza B, Meunier A (1993) Compact bone: numerical simulation of mechanical characteristics. *J Biomech* 26:677–687
- Dormieux L, Molinari A, Kondo D (2002) Micromechanical approach to the behavior of poroelastic materials. *J Mech Phys Solids* 50:2203–2231
- Fritsch A, Hellmich C, Dormieux L (2009) Ductile sliding between mineral crystals followed by rupture of collagen crosslinks: experimentally supported micromechanical explanation of bone strength. *J Theor Biol* 260:230–252
- Grimal Q, Parnell W (2011) Bonhomme, a homogenization code in MATLAB. [http://www.labos.upmc.fr/lip/IMG/gz/BonHom\\_V1-2-tar.gz](http://www.labos.upmc.fr/lip/IMG/gz/BonHom_V1-2-tar.gz)
- Grimal Q, Raum K, Gerisch A, Laugier P (2008) Derivation of the mesoscopic elasticity tensor of cortical bone from quantitative impedance images at the micron scale. *Comput Methods Biomed Eng* 11(2):147–157
- Hamad E, Lee Y, Jasiuk I (2010) Multiscale modeling of elastic properties of cortical bone. *Acta Mech* 213:131–154
- Hashin Z (1965) On elastic behavior of fibre reinforced materials of arbitrary transverse phase geometry. *J Mech Phys Solids* 13:119–134
- Hashin Z (1979) Analysis of properties of fiber composites with anisotropic constituents. *ASME J Appl Mech* 46:543–550
- Hashin Z, Rosen B (1964) The elastic moduli of fiber-reinforced materials. *ASME J Appl Mech* 31:223–232
- Hellmich C, Kober C, Erdmann B (2008) Micromechanics-based conversion of ct data into anisotropic elasticity tensors, applied to fe simulations of a mandible. *Ann Biomed Eng* 36:108–122
- Hellmich C, Ulm F-J, Dormieux L (2004) Can the diverse elastic properties of trabecular and cortical bone be attributed to only a few tissue-independent phase properties and their interactions? Arguments from a multiscale approach. *Biomech Model Mechanobiol* 2(4):219–238
- Hill R (1963) Elastic properties of reinforced solids: some theoretical principles. *J Mech Phys Solids* 11:357–372
- Hofmann T, Heyroth F, Meinhard H, Fränzel W, Raum K (2006) Assessment of composition and anisotropic elastic properties of secondary osteon lamellae. *J Biomech* 39(12):2282–2294
- Katz J (1980) Anisotropy of Young's modulus of bone. *Nature* 283:106–107
- Lowet G, van der Perre G (1996) Ultrasound velocity measurements in long bones: measurement method and simulation of ultrasound wave propagation. *J Biomech* 29:1255–1262
- Lydzba D, Shao D (2000) Study of poroelasticity material coefficients as response of microstructure. *Mech Cohesive Frict Mater* 5:149–171
- Markov K (1999) Elementary micromechanics of heterogeneous media. In: Markov K, Preziosi L (eds) *Heterogeneous media. Micromechanics modeling methods and simulations*. Birkhauser, Boston
- Mura T (1991) *Micromechanics of defects in solids*. Kluwer, Dordrecht
- Parnell W, Abrahams I (2006) Dynamic homogenization in periodic fibre reinforced media. Quasi-static limit for SH waves. *Wave Motion* 43:474–498
- Parnell W, Abrahams I (2008) Homogenization for wave propagation in periodic fibre-reinforced media with complex microstructure. I-Theory. *J Mech Phys Solids* 56:2521–2540
- Parnell W, Grimal Q (2009) The influence of mesoscopic porosity on cortical bone anisotropy. Investigations via asymptotic homogenization. *J R Soc Interface* 6:97–109
- Parton V, Kudryavtsev B (1993) *Engineering mechanics of composite structures*. CRC Press, Boca Raton
- Ponte-Castaneda P, Willis J (1995) The effect of spatial distribution on the effective behaviour of composite materials and cracked media. *J Mech Phys Solids* 43:1919–1951
- Rho J (1996) An ultrasonic method for measuring the elastic properties of human tibial cortical and cancellous bone. *Ultrasonics* 34:777–783
- Rodriguez R, Guinovart-Diaz R, Bravo-Castillero J, Sabina F, Berger H, Kari H, Gabbert U (2009) Variational bounds for anisotropic elastic multiphase composites with different shapes of inclusions. *Arch Appl Mech* 79:695–708
- Rohan E, Cimrman R (2011) Multiscale fe simulation of diffusion-deformation processes in homogenized dual-porous media. *Math Comput Simul* (in press)
- Sansalone V, Naili S, Bousson V, Bergot C, Peyrin F, Zarka J, Laredo J, Häiat G (2010) Determination of the heterogeneous anisotropic elastic properties of human femoral bone: from nanoscopic to organ scale. *J Biomech* 43:1857–1863
- Sokolnikoff I (1956) *Mathematical theory of elasticity*, 2nd edn. McGraw-Hill, New York
- Thomas C, Feik S, Clement J (2005) Regional variation of intracortical porosity in the midshaft of the human femur: age and sex differences. *J Anat* 206:115–125



- Turner C (2002) Biomechanics of bone: determinants of skeletal fragility and bone quality. *Osteoporos Int* 13:97–104
- Yoon H, Katz J (1976) Ultrasonic wave propagation in human cortical bone. I-theoretical considerations for hexagonal symmetry. *J Biomech* 9:407–412
- Yoon H, Katz J (1976) Ultrasonic wave propagation in human cortical bone. II-measurements of elastic properties and microhardness. *J Biomech* 9:459–464
- Yosibash Z, Trabelsi N, Hellmich C (2008) Subject-specific p-fe analysis of the proximal femur utilizing micromechanics-based material properties. *Int J Multiscale Comput Eng* 6:483–498
- Zysset P, Guo X, Hoffer C, Moore K, Goldstein S (1999) Elastic modulus and hardness of cortical and trabecular bone lamellae measured by nanoindentation in the human femur. *J Biomech* 32:1005–1012

Reproduced with permission of the copyright owner. Further reproduction prohibited without permission.